Measurements of the cross sections of $e^+e^- \to \Sigma_c\bar{\Sigma}_c$ and $\Lambda_c^+\bar{\Sigma}_c^-$ near kinematic thresholds

M. Ablikim *et al.*[*]

(BESIII Collaboration)

Based on e^+e^- annihilation data collected with the BESIII detector at the BEPCII collider, searches for the $e^+e^- \to \Sigma_c\bar{\Sigma}_c$ ($\Sigma_c^+\bar{\Sigma}_c^-$, $\Sigma_c^0\bar{\Sigma}_c^0$, and $\Sigma_c^{++}\bar{\Sigma}_c^{--}$) processes, as well as for the process $e^+e^- \to \Lambda_c^+\bar{\Sigma}_c^-$, are conducted for the first time at $\sqrt{s} = 4.750$, 4.781, 4.843, 4.918, and 4.951 GeV. As no signals are observed for all the above channels, the upper limits on their Born cross sections at the 90% confidence level are reported. The obtained upper limits of cross sections for $e^+e^- \to \Sigma_c\bar{\Sigma}_c$ are more than 2 orders of magnitude smaller than those for $e^+e^- \to \Lambda_c^+\bar{\Lambda}_c^-$ near the threshold. In contrast, such suppression is absent in hyperon pair production ($e^+e^- \to \Lambda\bar{\Lambda}$ and $\Sigma\bar{\Sigma}$), suggesting distinct underlying dynamics in charmed baryon production.

DOI: 10.1103/bjr6-rrdc

I. INTRODUCTION

In the quark model [1], baryons are not point-like particles but are described as being composed of three quarks. Although this model offers a valuable framework for understanding baryon structures, unresolved issues, such as the significant discrepancy between the proton mass and the sum of its three constituent quark masses [2], call for a critical reexamination of the quark model and highlight the need to better understand the interactions between the quarks inside the baryon.

The baryon properties can be indirectly examined through electron-positron collisions, where the two particles annihilate into a virtual photon, which converts into a baryon pair. The production cross section is parametrized in terms of electromagnetic form factors or effective form factors [3]. Hence, the measurement of the production cross sections of baryon pairs near the mass threshold provides valuable insights into the internal structure of baryons [4].

The production cross sections and (effective) form factors have been studied in different experiments [5–13], revealing several unexpected behaviors. For instance, in the hyperon sector, the cross sections of $e^+e^- \to \Sigma^-\bar{\Sigma}^+$, $e^+e^- \to \Sigma^+\bar{\Sigma}^-$, and $e^+e^- \to \Sigma^0\bar{\Sigma}^0$ are well described by perturbative quantum chromodynamics (pQCD) and follow a power law as a function of the energy [14,15],

while anomalous behaviors are observed for the $\Lambda\bar{\Lambda}$ [9] and $\Lambda\bar{\Sigma}^0$ [16] cross sections, which differ from the pQCD predictions at threshold. Specifically, a threshold enhancement larger than that predicted by pQCD is observed for $\Lambda\bar{\Lambda}$ and $\Lambda\bar{\Sigma}^0$.

With respect to the cross sections of charmed baryons, the Belle Collaboration initially reported a resonant structure consistent with the $Y(4660)$ state near the $\Lambda_c^+\bar{\Lambda}_c^-$ mass threshold [17]. In contrast, the BESIII Collaboration conducted a precise measurement of the cross sections of $e^+e^- \to \Lambda_c^+\bar{\Lambda}_c^-$ from threshold to 4.951 GeV, observed a threshold enhancement, and extracted the corresponding form factors [18,19], but with no indication of the resonant structure [19].

The study of the production cross sections of isospin-1 charmed baryon Σ_c pairs is of particular interest. First, the Σ_c baryon, including the three isospin partners Σ_c^0 (ddc), Σ_c^+ (udc), and Σ_c^{++} (uuc), has a considerable mass difference with respect to the Λ_c^+ (udc) [20,21], even though they present similar quark components. This mass difference can be interpreted as the energy difference between the heavier "bad" diquark $(ud)_{\text{spin}=1}$, which is symmetric in light quark spin, and the lighter "good" diquark $(ud)_{\text{spin}=0}$, which is antisymmetric [22]. Considering the $\Lambda_c^+\bar{\Lambda}_c^-$ and $\Sigma_c^+\bar{\Sigma}_c^-$ production, if the hadronization from the $c\bar{c}$ pair proceeds via attaching diquarks (ud), the cross section of the $e^+e^- \to \Lambda_c^+\bar{\Lambda}_c^-$ process is greater than the $e^+e^- \to \Sigma_c^+\bar{\Sigma}_c^-$ one, since the "bad" diquark is heavier than the "good" one, and the cross section is inversely proportional to the mass. Therefore, measuring the Σ_c^+ pair cross section is crucial for understanding the characteristics of "bad" and "good" diquarks, thereby to get insight into the inner structure of charmed baryons.

[*]Full author list given at the end of the article.

Second, it is of interest to explore whether the Σ_c pair can form a novel bound state, namely a dibaryon. Theories have various explanations for Σ_c-$\bar{\Sigma}_c$ interaction and have made predictions about potential new molecular states from both the hadron level and quark level. On the hadron level, several coupled channel effects, such as the one-pion-exchange model [23], the one-boson-exchange model [24,25], the single-channel Bethe-Salpeter equation [26], and the chiral perturbation theory [27,28] have been developed. On the quark level, theoretical approaches like the chiral quark model [29], quark delocalization color screening model [30], and lattice QCD [31] are employed to investigate bound-state production mechanisms. Despite the wealth of predictions, the mechanisms influencing the Σ_c-$\bar{\Sigma}_c$ interaction remain inadequately explored in the absence of experimental data, and it is essential to conduct relevant measurements to validate these predictions.

The hadron-hadron interactions and the potential dibaryon for the $\Lambda_c^+ \bar{\Sigma}_c^-$ system are also under discussion [25,30,32] and can be tested in the process $e^+e^- \to \Lambda_c^+ \bar{\Sigma}_c^-$, whose experimental studies are lacking. Moreover, isospin violation $|\Delta I| = 1$ is expected to manifest via $e^+e^- \to \gamma^* \to q\bar{q}$ (q denotes u, d, and s) in electromagnetic interaction. That raises concern regarding the relative amplitudes between $|\Delta I| = 0$ and $|\Delta I| = 1$ processes in charmed baryon production. In the $|\Delta I| = 1$ process $\gamma^* \to q\bar{q}$, under the diquark model, the diquark is initially produced and subsequently attaches to c or $\bar{c}$ during the hadronization process, resulting in a suppressed cross section compared to the $e^+e^- \to \Lambda_c^+ \bar{\Lambda}_c^-$ process. Thus, the measurement of the cross section ratio between $e^+e^- \to \Lambda_c^+ \bar{\Lambda}_c^-$ and $e^+e^- \to \Lambda_c^+ \bar{\Sigma}_c^-$ can shed light on the dynamics of the charmed baryon production and help to probe their inner structure from an alternative perspective.

In this paper, the aim is to measure the cross sections of $e^+e^- \to \Sigma_c \bar{\Sigma}_c$ ($\Sigma_c \bar{\Sigma}_c$ denotes $\Sigma_c^+ \bar{\Sigma}_c^-$, $\Sigma_c^0 \bar{\Sigma}_c^0$, or $\Sigma_c^{++} \bar{\Sigma}_c^{--}$) and $e^+e^- \to \Lambda_c^+ \bar{\Sigma}_c^-$ in the energy regions near their mass thresholds. The analyzed data samples were collected with the BESIII detector at BEPCII collider. The data samples taken at $\sqrt{s} = 4.918$ and 4.951 GeV, are utilized to measure the $e^+e^- \to \Sigma_c \bar{\Sigma}_c$ cross section. Subsequently, these data, along with those at $\sqrt{s} = 4.750$, 4.781, and 4.843 GeV, are utilized to conduct the latter measurement. The center-of-mass energies and integrated luminosities of these samples are measured from $e^+e^- \to \Lambda_c^+ \bar{\Lambda}_c^-$ and Bhabha events, respectively [33], with the specific values shown in Table I. Four Λ_c^+ Cabibbo-favored decay modes, namely, $\Lambda_c^+ \to pK_S^0, \Lambda_c^+ \to pK^-\pi^+, \Lambda_c^+ \to \Lambda\pi^+$, and $\Lambda_c^+ \to \Sigma^0\pi^+$, are employed to reconstruct the Λ_c^+, while the Σ_c is reconstructed by combining one residual pion with one Λ_c^+. Unless otherwise specified, charge-conjugate modes are always included.

The measurement of the $e^+e^- \to \Sigma_c \bar{\Sigma}_c$ cross section encounters several challenges. First, it is difficult to

TABLE I.   Summary of the c.m. energy and integrated luminosities of the data samples. All values are from Ref. [33], where the first uncertainty represents statistical uncertainty, and the second one represents systematic uncertainty.

$\sqrt{s}$ (MeV)	Luminosity (pb^{-1})
$4750.05 \pm 0.12 \pm 0.29$	$366.55 \pm 0.10 \pm 1.95$
$4780.54 \pm 0.12 \pm 0.30$	$511.47 \pm 0.12 \pm 2.72$
$4843.07 \pm 0.30 \pm 0.32$	$525.16 \pm 0.12 \pm 2.79$
$4918.02 \pm 0.34 \pm 0.34$	$207.82 \pm 0.08 \pm 1.10$
$4950.93 \pm 0.36 \pm 0.38$	$159.28 \pm 0.07 \pm 0.85$

disentangle the substantial contributions from $e^+e^- \to \Lambda_c^+ \bar{\Lambda}_c^{*-}(2595)$ and $e^+e^- \to \Lambda_c^+ \bar{\Lambda}_c^{*-}(2625)$ to the signal candidates $\Sigma_c \bar{\Sigma}_c$, since they have overlapping kinematics and the same final states. Additionally, not only do the two background channels $e^+e^- \to \Lambda_c^+ \bar{\Lambda}_c^{*-}$ have significant contributions [34], but also the decay rates of $\Lambda_c^{*+} \to \Lambda_c^+ \pi\pi$ have large uncertainties [35]. To overcome these challenges, three types of data samples are selected, including one sample of singly tagged Λ_c^+ [36], three samples of reconstructing one Λ_c^+ along one π in three different charges, and two samples of combining a $\pi^+\pi^-$ or $\pi^0\pi^0$ with a Λ_c^+. To simplify, these strategies are abbreviated as "Tag Λ_c^+," "Tag $\Lambda_c^+\pi$," and "Tag $\Lambda_c^+\pi\pi$," respectively, throughout this paper. A simultaneous fit is carried out to the three types of samples to determine the cross sections of the signal channels. Furthermore, the "Tag Λ_c^+" sample is utilized to measure the cross section of the $e^+e^- \to \Lambda_c^+ \bar{\Sigma}_c^-$ process.

II. DETECTOR AND DATA SAMPLE

The BESIII detector [37] records symmetric e^+e^- collisions provided by the BEPCII storage ring [38], which operates in the c.m. energy range from 1.84 to 4.95 GeV. The cylindrical core of the BESIII detector covers 93% of the full solid angle and consists of a helium-based multilayer drift chamber (MDC), a plastic scintillator time-of-flight system (TOF), and a CsI(Tl) electromagnetic calorimeter (EMC), which are all enclosed in a superconducting solenoidal magnet providing a 1.0 T magnetic field. The solenoid is supported by an octagonal flux-return yoke with resistive plate counter muon identification modules interleaved with steel. The charged-particle momentum resolution at 1 GeV/c is 0.5%, and the dE/dx resolution is 6% for electrons from Bhabha scattering. The EMC measures photon energies with a resolution of 2.5% (5%) at 1 GeV in the barrel (end cap) region. The time resolution in the TOF barrel region is 68 ps, while that in the end cap region is 110 ps. In 2015, the end cap TOF was replaced with a multigap resistive plate chamber, and the time resolution improved to 60 ps. All datasets mentioned in this paper benefit from this upgrade.

Monte Carlo (MC) simulated data samples produced with a GEANT4-based [39] software package, which includes the geometric description of the BESIII detector and the detector response, are used to determine detection efficiencies and to estimate backgrounds. The simulation models the beam energy spread and initial state radiation (ISR) in the e^+e^- annihilations with the generator KKMC [40,41]. All particle decays are modeled with EVTGEN [42,43], using branching fractions either taken from the Particle Data Group [35], when available, or otherwise estimated with LUNDCHARM [44,45]. Final-state radiation from charged final-state particles is incorporated using the PHOTOS package [46].

The Λ_c^+ events in signal MC samples are generated according to the partial wave analysis result of $\Lambda_c^+ \to pK^-\pi^+$ [47] and considering the polarization effects seen in data for the $\Lambda_c^+ \to pK_S^0$, $\Lambda_c^+ \to \Lambda\pi^+$, and $\Lambda_c^+ \to \Sigma^0\pi^+$ channels [48,49]. The $\Sigma_c \to \Lambda_c^+\pi$ is assumed as the only decay mode of Σ_c.

The primary background sources include $e^+e^- \to \Lambda_c^+\bar{\Lambda}_c^{*-}(2595)$, $e^+e^- \to \Lambda_c^+\bar{\Lambda}_c^{*-}(2625)$, $e^+e^- \to \Lambda_c^+\bar{\Sigma}_c\pi$ ($\Lambda_c^+\bar{\Sigma}_c^0\pi^-$, $\Lambda_c^+\bar{\Sigma}_c^{--}\pi^+$, $\Lambda_c^+\bar{\Sigma}_c^-\pi^0$), $e^+e^- \to \Lambda_c^+\bar{\Lambda}_c^-$, and hadronic backgrounds. To estimate their contributions, the corresponding exclusive MC samples are also generated. For $\Lambda_c^{*+}(2595)$ and $\Lambda_c^{*+}(2625)$, only the strong decays, specifically $\Lambda_c^{*+} \to \Sigma_c^0\pi^+$, $\Sigma_c^+\pi^0$, $\Sigma_c^{++}\pi^-$, $\Lambda_c^+\pi^+\pi^-$, and $\Lambda_c^+\pi^0\pi^0$, are considered in the simulation with uniform kinematic distributions. Each of the five Λ_c^{*+} decay channels is simulated in equal proportions, and the relative ratio among the different decay channels is adjusted for further studies. For other hadronic backgrounds, the hadronic inclusive MC sample is simulated, including $D_{(s)}^{(*)}$ pair production, ISR return to the charmonium and charmonium-like ψ states at lower masses, and continuum processes $e^+e^- \to q\bar{q}$.

III. Λ_c^+ RECONSTRUCTION

The Λ_c^+ reconstruction is performed through final states characterized by p, $K_S^0(\to \pi^+\pi^-)$, K, π, $\Lambda(\to p\pi^-)$, and $\Sigma^0(\to \Lambda\gamma)$ particles.

Charged tracks detected in the MDC are required to be within a polar angle (θ) range of $|\cos\theta| < 0.93$, where θ is defined with respect to the z axis, which is the symmetry axis of the MDC. For charged tracks not originating from K_S^0, Λ or Σ^0 decays, the distance of closest approach to the interaction point (IP) must be less than 10 cm along the z axis, $|V_z|$, and less than 1 cm in the transverse plane, $|V_{xy}|$.

Particle identification (PID) for charged tracks combines measurements of the energy deposited in the MDC (dE/dx) and the flight time in the TOF to form likelihoods $\mathcal{L}(h)(h = p, K, \pi)$ for each hadron h hypothesis. Tracks are identified as protons when the proton hypothesis has

the greatest likelihood [$\mathcal{L}(p) > \mathcal{L}(K)$ and $\mathcal{L}(p) > \mathcal{L}(\pi)$], while charged kaons and pions are identified by comparing the likelihoods for the kaon and pion hypotheses, $\mathcal{L}(K) > \mathcal{L}(\pi)$ and $\mathcal{L}(\pi) > \mathcal{L}(K)$, respectively. These criteria are not applied for tracks used in reconstructing K_S^0 or to the π^- candidates for the Λ decay.

Photon candidates are identified using isolated showers in the EMC. The deposited energy of each shower must be greater than 25 MeV in the barrel region ($|\cos\theta| < 0.80$) and more than 50 MeV in the end-cap region ($0.86 < |\cos\theta| < 0.92$). To suppress electronic noise and showers unrelated to the event, the difference between the EMC time and the event start time is required to be within [0, 700] ns.

The K_S^0 and Λ candidates are reconstructed from two oppositely charged tracks satisfying $|V_z| < 20$ cm, the $\pi^+\pi^-$ and $p\pi^-$ final states, respectively. The two tracks are constrained to originate from a common decay vertex, with a requirement on the χ^2 of the vertex fit being less than 100. Additionally, the decay length of the candidates is required to be greater than twice the vertex resolution away from the IP. The Σ^0 candidates are reconstructed by combining Λ candidates with a photon. The four-momenta of K_S^0 and Λ candidates are updated according to the vertex fits. Signal mass windows are defined as $487 \text{ MeV}/c^2 < M(\pi^+\pi^-) < 511 \text{ MeV}/c^2$, $1111 \text{ MeV}/c^2 < M(p\pi^-) < 1121 \text{ MeV}/c^2$, and $1179 \text{ MeV}/c^2 < M(\Lambda\gamma) < 1203 \text{ MeV}/c^2$ to select the K_S^0, Λ, and Σ^0 signal candidates, respectively.

To further improve the Λ_c^+ signal resolution, a vertex fit is performed on all charged tracks (including tracks of long-lived particles) to constrain them to one common vertex. Events with a fit quality of $\chi^2 < 200$ are selected as candidate events.

IV. MEASUREMENTS OF $e^+e^- \to \Sigma_c\bar{\Sigma}_c$ CROSS SECTION

A. Event selection

1. Tag Λ_c^+ sample

Among all the Λ_c^+ candidates reconstructed in an event, only the one yielding the minimum $|\Delta M| = |M(\Lambda_c^+) - m(\Lambda_c^+)|$ value is retained for subsequent analysis, where $M(\Lambda_c^+)$ represents the reconstructed invariant mass of the Λ_c^+ candidate and $m(\Lambda_c^+)$ is the known Λ_c^+ mass [35]. Furthermore, the requirement $|\Delta M| < 0.02 \text{ GeV}/c^2$ is applied to reject the non-Λ_c^+ background. The value $RM(\Lambda_c^+) + M(\Lambda_c^+) - m(\Lambda_c^+)$, corresponding to the Λ_c^+ recoil mass $RM(\Lambda_c^+)$ subtracted by the Λ_c^+ mass resolution, must exceed $2.54 \text{ GeV}/c^2$ to exclude processes like $e^+e^- \to \Lambda_c^+\bar{\Lambda}_c^-$ and $e^+e^- \to \Lambda_c^+\bar{\Sigma}_c^-$, where $RM(\Lambda_c^+) = |P_{e^+e^-} - P_{\Lambda_c^+}|/c$, and $P_{e^+e^-}$ and $P_{\Lambda_c^+}$ represent the four-momenta of the e^+e^- system and Λ_c^+ in the laboratory frame, respectively.

2. Tag $\Lambda_c^+ \pi$ sample

The Λ_c^+ candidates are combined with residual π^+, π^-, or π^0 to form Σ_c candidates. The π^0 candidates are reconstructed from photon pairs with invariant masses $M(\gamma\gamma)$ ranging from 115 MeV/c^2 to 150 MeV/c^2. To improve the momentum resolution, a kinematic fit constraining the invariant mass of the photon pairs to the π^0 known mass [35] is performed, and the resulting four-momentum of the π^0 candidate is utilized for further analysis.

After applying the Λ_c^+ mass window requirement, $M(\Lambda_c^+) \in (2.275, 2.300)$ GeV/c^2, the optimal $\Lambda_c^+ \pi$ candidate is selected by minimizing the variable $\Delta E(\Lambda_c^+ \pi) = E_{\mathrm{CMS}} - E(\Lambda_c^+ \pi) - E_{\mathrm{rec}}(\Lambda_c^+ \pi)$, where E_{CMS} represents the total energy of the initial e^+e^- collisions; $E(\Lambda_c^+ \pi)$ is the total energy of Λ_c^+ and π; and $E_{\mathrm{rec}}(\Lambda_c^+ \pi) = \sqrt{p_{\Lambda_c^+ \pi}^2 c^2 + m(\Sigma_c)^2 c^4}$, where $p_{\Lambda_c^+ \pi}$ is the total momentum of Λ_c^+ and π, and $m(\Sigma_c)$ is the known Σ_c mass [35]. In order to suppress wrong combinations and the hadronic background, $\Delta E(\Lambda_c^+ \pi)$ is required to be greater than -0.018 GeV. This criterion also improves the $\Lambda_c^+ \bar{\Lambda}_c^{*-}$ resolution with minimal signal efficiency loss. To take advantage of the accuracy of the beam energy E_{beam} measurement [33], the beam-constrained mass $M_{\mathrm{BC}}(\Lambda_c^+ \pi)c^2 = \sqrt{E_{\mathrm{beam}}^2 - p_{\Lambda_c^+ \pi}^2 c^2}$ is used for the subsequent fit.

3. Tag $\Lambda_c^+ \pi\pi$ sample

This sample is formed by combining the residual $\pi^+\pi^-$ or $\pi^0\pi^0$ pairs with a Λ_c^+ candidate. The variable $\Delta E(\Lambda_c^+ \pi\pi) = E_{\mathrm{CMS}} - E(\Lambda_c^+ \pi\pi) - E_{\mathrm{rec}}(\Lambda_c^+ \pi\pi)$ is constructed to select the optimal $\Lambda_c^+ \pi\pi$ candidates, where $E(\Lambda_c^+ \pi\pi)$ is the total energy of Λ_c^+ and $\pi\pi$, and $E_{\mathrm{rec}}(\Lambda_c^+ \pi\pi) = \sqrt{p_{\Lambda_c^+ \pi\pi}^2 c^2 + m(\Lambda_c^+)^2 c^4}$. The condition $\Delta E(\Lambda_c^+ \pi\pi) > -0.02$ GeV is required for background suppression, and signal candidates with $RM(\Lambda_c^+ \pi\pi) + M(\Lambda_c^+) - m(\Lambda_c^+)$ within the range $(2.26, 2.31)$ GeV/c^2 are retained to identify the $\bar{\Lambda}_c^-$ on the recoil side.

B. Simultaneous fit

An unbinned maximum likelihood fit is performed on the distributions across all the tagged samples and energy points. Explicitly, the fit comprises three forms: a 1D fit to the $RM(\Lambda_c^+) + M(\Lambda_c^+) - m(\Lambda_c^+)$ distribution in the "Tag Λ_c^+" sample, a 2D fit to the $M_{\mathrm{BC}}(\Lambda_c^+ \pi)$ versus $RM(\Lambda_c^+) + M(\Lambda_c^+) - m(\Lambda_c^+)$ distribution in the "Tag $\Lambda_c^+ \pi$" samples, and a 2D fit to the $M(\Lambda_c^+ \pi\pi) - M(\Lambda_c^+) + m(\Lambda_c^+)$ versus $RM(\Lambda_c^+) + M(\Lambda_c^+) - m(\Lambda_c^+)$ distribution in the "Tag $\Lambda_c^+ \pi\pi$" samples. The yields of signal processes at each energy point are constrained to their observed cross sections, with the branching fractions of $\Lambda_c^{*+} \to \Lambda_c^+ \pi\pi$ as shared parameters across different energy points.

The observed cross sections are determined by

$$\sigma_{\mathrm{obs}} = \frac{N_{\mathrm{fit}}(\mathrm{Tag\ X})}{2 \times \mathcal{L}_{\mathrm{int}} \times \epsilon_{\mathrm{tot}}(\mathrm{Tag\ X})}, \quad (1)$$

where $N_{\mathrm{fit}}(\mathrm{Tag\ X})$ represents the fitted yield in the "Tag Λ_c^+" and "Tag $\Lambda_c^+ \pi$" samples, and $\mathcal{L}_{\mathrm{int}}$ denotes the integrated luminosity obtained from Ref. [33]. $\epsilon_{\mathrm{tot}}(\mathrm{Tag\ X}) = \sum_{i=1}^{4} \epsilon_i(\mathrm{Tag\ X}) \times \mathcal{B}_i$ is the sum of the products of the detection efficiency $\epsilon_i(\mathrm{Tag\ X})$ in the "Tag X" sample and the corresponding branching fraction $\mathcal{B}_i$ for the ith Λ_c^+ tag mode [35]. Notably, the detection efficiencies include the branching fractions of the Λ_c^+ daughter particles and represent the average efficiencies of Λ_c^+ and $\bar{\Lambda}_c^-$.

Considering the ratio between the yields of Λ_c^{*+} in "Tag $\Lambda_c^+ \pi\pi$" samples $N_{\mathrm{fit}}^{\Lambda_c^{*+}}(\mathrm{Tag\ } \Lambda_c^+ \pi\pi)$ and "Tag Λ_c^+" samples $N_{\mathrm{fit}}^{\Lambda_c^{*+}}(\mathrm{Tag\ } \Lambda^+)$, along with the efficiency, the inclusive branching fractions of $\Lambda_c^{*+} \to \Lambda_c^+ \pi^+\pi^-$ and $\Lambda_c^{*+} \to \Lambda_c^+ \pi^0\pi^0$ can be formulated as follows:

$$\mathcal{B}(\Lambda_c^{*+} \to \Lambda_c^+ \pi\pi) = \frac{\mathcal{A}^{\Lambda_c^{*+}}(\mathrm{Tag\ } \Lambda_c^+ \pi\pi)}{\mathcal{A}^{\Lambda_c^{*+}}(\mathrm{Tag\ } \Lambda_c^+)}, \quad (2)$$

where $\mathcal{A}^{\Lambda_c^{*+}} = N_{\mathrm{fit}}^{\Lambda_c^{*+}}/\epsilon_{\mathrm{tot}}^{\Lambda_c^{*+}}$.

Since the use of simultaneous fit is not able to constrain the large number of free parameters with the current statistics, the isospin symmetry of the following cross sections are assumed: i.e., $\sigma_{\mathrm{obs}}(e^+e^- \to \Sigma_c^+ \bar{\Sigma}_c^-) = \sigma_{\mathrm{obs}}(e^+e^- \to \Sigma_c^0 \bar{\Sigma}_c^0) = \sigma_{\mathrm{obs}}(e^+e^- \to \Sigma_c^{++} \bar{\Sigma}_c^{--})$, and $\sigma_{\mathrm{obs}}(e^+e^- \to \Lambda_c^+ \bar{\Sigma}_c^0 \pi^-) = \sigma_{\mathrm{obs}}(e^+e^- \to \Lambda_c^+ \bar{\Sigma}_c^- \pi^+) = \sigma_{\mathrm{obs}}(e^+e^- \to \Lambda_c^+ \bar{\Sigma}_c^- \pi^0)$. In addition, according to Refs. [35,50], the branching fraction ratios of the subprocesses $\Lambda_c^*(2595)^+(\Lambda_c^*(2625)^+) \to \Sigma_c^0 \pi^+$, $\Sigma_c^{++} \pi^-$, and $\Lambda_c^+ \pi^+\pi^-$ (three-body decay) are assumed to be 0.36 (0.08), 0.36 (0.08), and 0.28 (0.84), respectively, to the inclusive branching fraction of $\Lambda_c^{*+} \to \Lambda_c^+ \pi^+\pi^-$. Similarly, for the final state $\Lambda_c^+ \pi^0\pi^0$, the ratios are assumed to be 0.71 (0.15) for $\Lambda_c^{*+} \to \Sigma_c^+ \pi^0$ and 0.29 (0.85) for $\Lambda_c^+ \pi^0\pi^0$ (three-body decay). The constraints will be factored into the efficiency estimation and the construction of the signal model.

The signal shapes are obtained from MC simulations convolved with Gaussian functions, to take into account the resolution discrepancy between data and MC simulations. The parameters of the Gaussian functions on different dimensions are fixed according to studies with control samples. In the $RM(\Lambda_c^+) + M(\Lambda_c^+) - m(\Lambda_c^+)$ distribution, the data control samples $e^+e^- \to \Lambda_c^+ \bar{\Lambda}_c^-$ at $\sqrt{s} = 4.600$, 4.612, and 4.641 GeV are used to assess the resolution discrepancy in the signal process, based on the tagged Λ_c^+ momentum. The same method is used to estimate the resolution discrepancy in the $M_{\mathrm{BC}}(\Lambda_c^+ \pi)$ distributions. The resolution discrepancy in the $M(\Lambda_c^+ \pi\pi) - M(\Lambda_c^+) + m(\Lambda_c^+)$ distributions is evaluated by analyzing the decay
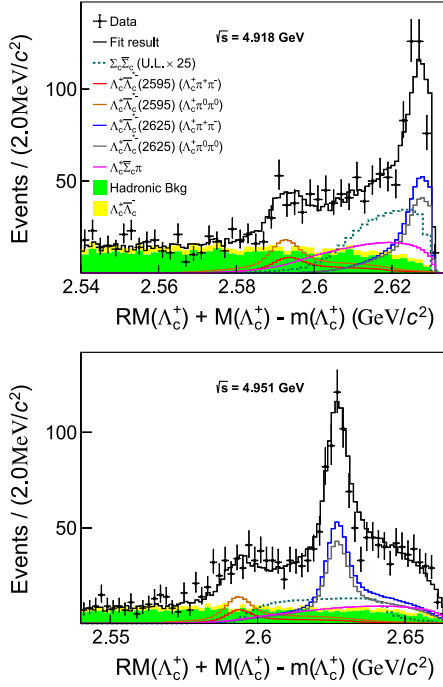
FIG. 1. One-dimensional fit results at $\sqrt{s} = 4.918$ GeV (top) and $\sqrt{s} = 4.951$ GeV (bottom) in the "Tag Λ_c^+" sample. The dots with error bars denote data, and the black solid curves correspond to the fit result. "Bkg" stands for the background. The dashed lines represent the MC distributions of the components $\Sigma_c^+\bar{\Sigma}_c^-$, $\Sigma_c^0\bar{\Sigma}_c^0$, and $\Sigma_c^{++}\bar{\Sigma}_c^{--}$. "U.L. $\times$ 25" indicates the MC distribution normalized to 25 times the 90% confidence level upper limit of the $\Sigma_c\bar{\Sigma}_c$ observed cross section.

$\psi(3686) \to \pi\pi J/\psi$, $J/\psi \to \rho\pi$. Gaussian functions in the $M(J/\psi\pi\pi) - M(J/\psi) + m(J/\psi)$ spectra are employed to characterize the resolution effect of the signal process, with $M(J/\psi\pi\pi)$, $M(J/\psi)$, and $m(J/\psi)$ representing the invariant mass of $J/\psi\pi\pi$ and J/ψ, and the known mass of J/ψ [35], respectively.

The backgrounds from Λ_c^+ pair productions and non-Λ_c^+ hadronic backgrounds are evaluated according to the MC simulations. Their shapes are obtained from the corresponding MC samples. In the fit, the amplitudes of the Λ_c^+ pair backgrounds are fixed according to the BESIII measurement [19], while the contributions of hadronic backgrounds are scaled from MC simulations by a global factor across all tagged samples at a single energy point, which is left floating in the fit.

The fit results are illustrated in Figs. 1 and 2, where no $e^+e^- \to \Sigma_c\bar{\Sigma}_c$ signal is present at either $\sqrt{s} = 4.918$ GeV or $\sqrt{s} = 4.951$ GeV. Hence, the upper limits on the observed cross section $\sigma_{\text{U.L.}}$ at the 90% confidence level (CL) are obtained by solving the equation

$$\int_0^{\sigma_{\text{U.L.}}} \mathcal{L}(x)\mathrm{d}x = 0.9 \int_0^{\infty} \mathcal{L}(x)\mathrm{d}x, \qquad (3)$$

where x is the assumed cross section of $e^+e^- \to \Sigma_c\bar{\Sigma}_c$, and $\mathcal{L}(x)$ is the maximized likelihood of the data assuming a cross section of x.

Input/output (I/O) checks are performed to validate the fitting procedure and to evaluate the impact of statistical correlations among the simultaneously fitted data samples. Based on simulated MC samples, these tests assess (i) biases in the extracted cross sections, (ii) the effect of intersample correlations on the estimated uncertainties, and (iii) their influence on the upper limit determination. The I/O tests indicate that the fit underestimates the uncertainties and introduces small biases in the estimated cross sections, but the uncertainty underestimation has a negligible effect on the upper limit estimation. As a result, only the bias on x in Eq. (3) is considered.

The Born cross section is determined by

$$\sigma_{\text{Born}} = \frac{\sigma_{\text{U.L.}}}{f_{\text{VP}} \times f_{\text{ISR}}}, \qquad (4)$$

where the vacuum polarization (VP) correction factor f_{VP} is calculated to be 1.06 at all energy points [51]. The ISR correction factor f_{ISR} [52] is obtained from the KKMC generator and calculated as 0.96 at all energy points, assuming the input Born cross section is the same as that of $e^+e^- \to \Lambda_c^+\bar{\Lambda}_c^-$ [19].

C. Systematic uncertainty

The systematic uncertainties can be categorized into multiplicative and additive forms. Details are discussed in the following parts.

1. Multiplicative items

The sources of multiplicative uncertainties arise from Λ_c^+ reconstruction, branching fractions of the Λ_c^+ decay channels, integrated luminosity, tracking and PID of residual charged pions, reconstruction of residual π^0, MC statistics, f_{ISR}, and f_{VP}. Specifically, the uncertainties associated with the reconstructions of $\Lambda_c^+ \to pK_S^0$, $pK^-\pi^+$, $\Lambda\pi^+$, and $\Sigma^0\pi^+$, as detailed in Sec. III, are estimated as 2.0%, 3.9%, 2.4%, and 2.4%, respectively [53], while the uncertainties of branching fractions are assigned as 5.0%, 5.0%, 5.3%, and 5.4%, respectively [35]. According to Ref. [33], the uncertainties associated with the integrated luminosity are estimated as 0.5% for all energy points. The uncertainties in tracking and PID for residual charged pions are primarily dependent on the pions' momenta. Discrepancies in their efficiencies between data and MC simulation are determined to be 3.5% and 1.6%, respectively, from the analysis of pions with momenta below 0.2 GeV/c in the hadronic decays of D^0 and $D^\pm$ mesons. For the reconstruction of residual π^0, the uncertainty is assigned as 2.8%, according to the study of π^0 with momenta below 0.2 GeV in the
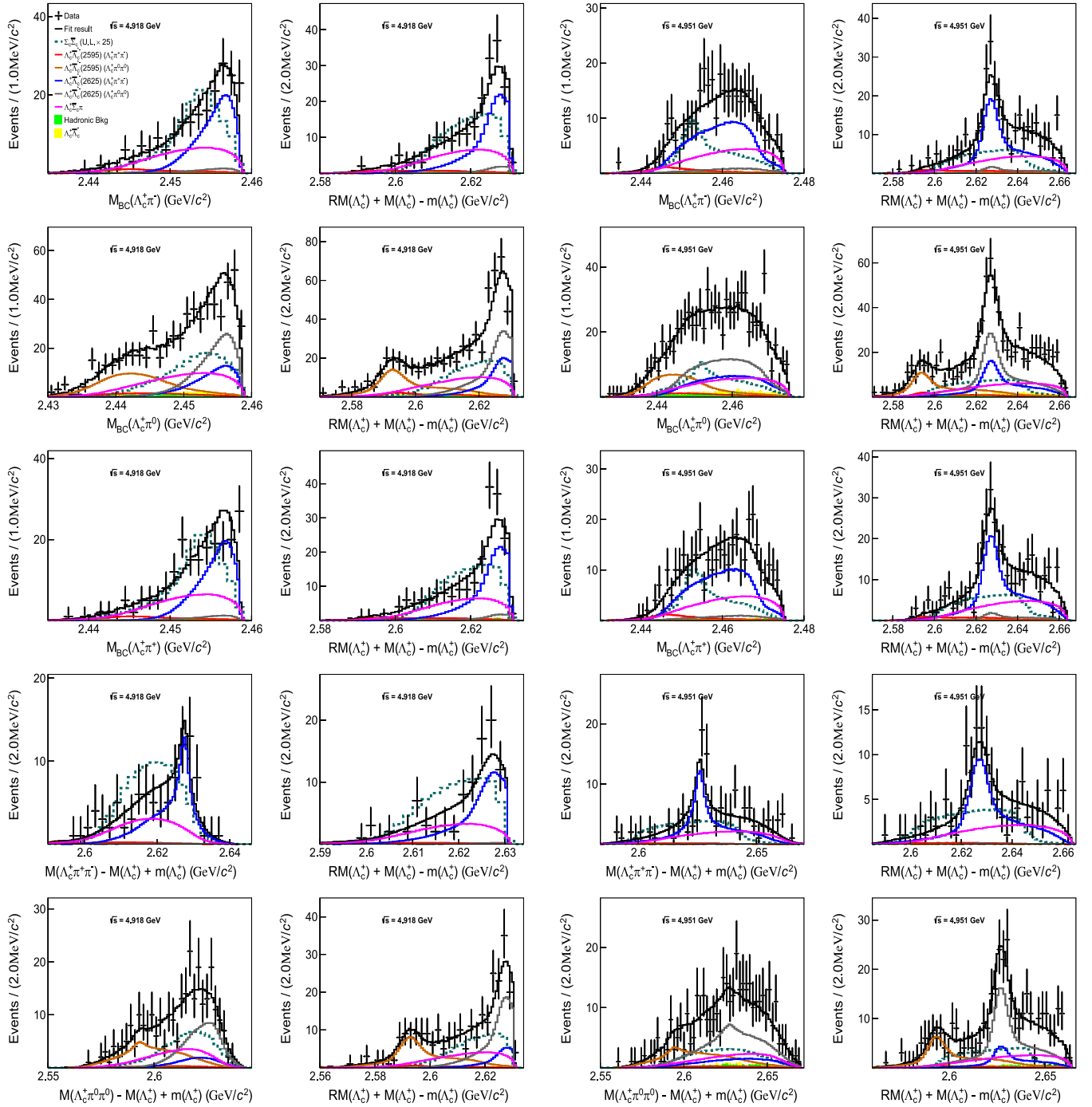
FIG. 2.   Two-dimensional fit results at $\sqrt{s} = 4.918$ and 4.951 GeV. The rows, from top to bottom, correspond to the results in the samples of "Tag $\Lambda_c^+\pi^-$", "Tag $\Lambda_c^+\pi^0$", "Tag $\Lambda_c^+\pi^+$", "Tag $\Lambda_c^+\pi^+\pi^-$", and "Tag $\Lambda_c^+\pi^0\pi^0$". The dots with error bars denote the data, while the black solid curves correspond to the total fit function. "Bkg" stands for the background. The dashed lines represent the MC distributions of the components $\Sigma_c^+\bar{\Sigma}_c^-$, $\Sigma_c^0\bar{\Sigma}_c^0$, and $\Sigma_c^{++}\bar{\Sigma}_c^{--}$. "U.L. $\times$ 25" indicates the MC distributions normalized to 25 times the 90% confidence level upper limit of the $\Sigma_c\bar{\Sigma}_c$ observed cross section.

control channel $D^0 \rightarrow K^-\pi^+\pi^0$. The uncertainty associated with MC statistics is 0.2% for all processes.

Several sources of systematic uncertainties are considered in the determination of f_{ISR}. First, the uncertainties arising from the model choice are estimated by employing

CONEXC [54] as an alternative algorithm. They are determined to be 6.9% and 0.1% at $\sqrt{s} = 4.918$ and 4.951 GeV, respectively. Subsequently, the uncertainty associated with the c.m. energy ($\sqrt{s}$) [33] is investigated by varying the input energy within its error range in the MC simulation.

TABLE II.   Summary of the multiplicative uncertainties (in %), except for f_{ISR} and f_{VP}. "Rec" is an abbreviation for reconstruction, while $\mathcal{B}$ denotes the branching fraction. "N/A" means that a term is not applicable to the corresponding sample.

| Sample | $\mathcal{L}_{int}$ | Λ_c^+ Rec $(\mathcal{B})$ | | | | π^+ Tracking | π^+ PID | π^0 Rec | MC statistics |
		pK_S^0	$pK^-\pi^+$	$\Lambda\pi^+$	$\Sigma^0\pi^+$				
Tag Λ_c^+	0.5	2.0 (5.0)	3.9 (5.0)	2.4 (5.3)	2.4 (5.4)	N/A	N/A	N/A	0.2
Tag $\Lambda_c^+\pi^\pm$	0.5	2.0 (5.0)	3.9 (5.0)	2.4 (5.3)	2.4 (5.4)	3.5	1.6	N/A	0.2
Tag $\Lambda_c^+\pi^0$	0.5	2.0 (5.0)	3.9 (5.0)	2.4 (5.3)	2.4 (5.4)	N/A	N/A	2.8	0.2
Tag $\Lambda_c^+\pi^+\pi^-$	0.5	2.0 (5.0)	3.9 (5.0)	2.4 (5.3)	2.4 (5.4)	7.0	3.2	N/A	0.2
Tag $\Lambda_c^+\pi^0\pi^0$	0.5	2.0 (5.0)	3.9 (5.0)	2.4 (5.3)	2.4 (5.4)	N/A	N/A	5.6	0.2

This uncertainty is quantified as 1.1% and 0.3% at $\sqrt{s} =$ 4.918 and 4.951 GeV, respectively. Similarly, the systematic uncertainty arising from the estimation of the beam energy spread [55] is determined to be 1.5% and 0.2% at $\sqrt{s} = 4.918$ and 4.951 GeV, respectively. The uncertainty related to the calculation of f_{VP} at all energy points is determined as 0.5% [51].

A summary of multiplicative uncertainties except for f_{ISR} and f_{VP} is presented in Table II, and they are the same at both energy points. A MC approach is employed to estimate the resultant effect on the fitted cross sections introduced by the systematic uncertainties, assuming a Gaussian distribution for each multiplicative uncertainty. The total multiplicative uncertainties are determined to be 13.1% and 8.1% for the Born cross section at $\sqrt{s} = 4.918$ and 4.951 GeV, respectively.

2. Additive items

The additive uncertainties consist of the line shape of the Born cross section for $e^+e^- \to \Sigma_c\bar{\Sigma}_c$, the polarization of $e^+e^- \to \Lambda_c^+\bar{\Lambda}_c^{*-}$, the polarization of $e^+e^- \to \Sigma_c\bar{\Sigma}_c$, isospin constraints among the cross sections of $e^+e^- \to \Lambda_c\bar{\Sigma}_c\pi$ and among the cross sections of $e^+e^- \to \Sigma_c\bar{\Sigma}_c$, and the correction for the difference in resolution between the simulated and real data samples.
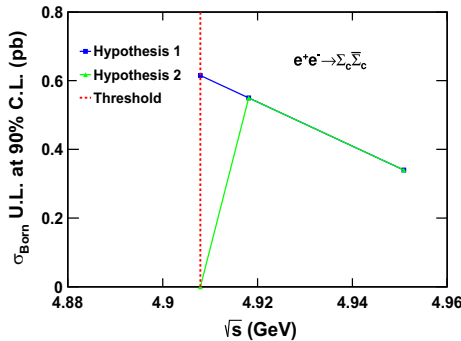
FIG. 3.   Upper limit at the 90% CL on the Born cross section of $e^+e^- \to \Sigma_c\bar{\Sigma}_c$. Points above the threshold represent the upper limit based on the assumed line shape of $e^+e^- \to \Lambda_c^+\bar{\Lambda}_c^-$, as shown in Table III. The blue and green curves represent alternative assumed line shapes.

The uncertainties in the cross section line shape arise from variations in the ISR correction. Given the absence of any observed signal and the lack of theoretical predictions, the baseline ISR correction factor (summarized in Table III) is computed using the measured $e^+e^- \to \Lambda_c^+\bar{\Lambda}_c^-$ cross section from Ref. [19]. Systematic uncertainties associated with the $e^+e^- \to \Sigma_c\bar{\Sigma}_c$ line shape are subsequently derived by analyzing line shapes under two new hypotheses. Hypothesis 1 holds that the production of $e^+e^- \to \Sigma_c\bar{\Sigma}_c$ exhibits a threshold enhancement, similar to cases such as $e^+e^- \to p\bar{p}$ [7] and $e^+e^- \to \Lambda_c^+\bar{\Lambda}_c^-$ [19]. Hypothesis 2 assumes no threshold enhancement effect, and it considers the most extreme scenario where the cross section is zero at the threshold. The line shapes that correspond to both hypotheses are represented in Fig. 3. The Born cross sections based on each hypothesis are presented in Table III. The comparison reveals that, under Hypothesis 2 in Table III, the upper-limit estimation of the $e^+e^- \to \Sigma_c\bar{\Sigma}_c$ Born cross section reaches its most conservative value. Thus, subsequent studies on additive systematic uncertainties are based on this scenario.

The potential impact of Λ_c^{*+} polarization is considered, as it can affect the detection efficiency and signal shape of $e^+e^- \to \Lambda_c^+\bar{\Lambda}_c^{*-}$, ultimately influencing the evaluation of $e^+e^- \to \Sigma_c\bar{\Sigma}_c$ signal yields. To evaluate the potential effect, the events in the signal phase-space MC samples are

TABLE III.   Summary of f_{VP}, f_{ISR}, and $\sigma_{Born}(e^+e^- \to \Sigma_c\bar{\Sigma}_c)$, based on different assumptions of line shapes: 1. baseline model adopting $e^+e^- \to \Lambda_c^+\bar{\Lambda}_c^-$ measurements from Ref. [19]; 2. threshold-enhanced hypothesis (Hypothesis 1); 3. nonenhanced scenario (Hypothesis 2). All upper limits are set at the 90% CL, and they do not include the systematic uncertainties.

$\sqrt{s}$	f	Baseline	Hypothesis 1	Hypothesis 2
4.918 GeV	f_{VP}	1.06	1.06	1.06
	f_{ISR}	0.96	0.68	0.58
	σ_{Born}	<0.55 pb	<0.61 pb	<0.83 pb
4.951 GeV	f_{VP}	1.06	1.06	1.06
	f_{ISR}	0.96	0.81	0.79
	σ_{Born}	<0.34 pb	<0.39 pb	<0.49 pb

weighted based on the angular distribution form $f(\theta) \propto 1 + \alpha_{\Lambda_c^+} \cos^2 \theta_{\Lambda_c^+}$ [18]. Here, $\theta_{\Lambda_c^+}$ is the polar angle of Λ_c^+ in the c.m. system of its mother particle Λ_c^{*+}. The parameter $\alpha_{\Lambda_c^+}$ quantifies the degree of polarization, obtained from Ref. [34]. In the same manner, the polarization effect of $e^+e^- \to \Sigma_c \bar{\Sigma}_c$ can be determined. However, there is no theoretical prediction or experimental observation as inputs. Hence, the extreme scenario is considered, with Σ_c being completely polarized at the two energy points—namely, $\alpha_{\Sigma_c} = \pm 1$.

To account for potential isospin symmetry-breaking effects, the ratios of $\sigma(e^+e^- \to \Lambda_c^+ \bar{\Sigma}_c^0 \pi^-)$, $\sigma(e^+e^- \to \Lambda_c^+ \bar{\Sigma}_c^{--} \pi^+)$, and $\sigma(e^+e^- \to \Lambda_c^+ \bar{\Sigma}_c^- \pi^0)$ are varied in two different cases: 1:1:0.5 and 1:1:2, and thereafter the upper limits are reestimated. Likewise, the ratios of $\sigma(e^+e^- \to \Sigma_c^+ \bar{\Sigma}_c^-)$, $\sigma(e^+e^- \to \Sigma_c^{++} \bar{\Sigma}_c^{--})$, and $\sigma(e^+e^- \to \Sigma_c^0 \bar{\Sigma}_c^0)$ are changed to 1:1:0.5 and 1:1:2.

The uncertainty due to resolution differences between simulation and data can affect the analysis. To evaluate the potential size, control samples of $e^+e^- \to \Lambda_c^+ \bar{\Lambda}_c^-$ at $\sqrt{s} = 4.918$ and 4.951 GeV are used to obtain the new parameters of Gaussian functions for the $RM(\Lambda_c^+) + M(\Lambda_c^+) - m(\Lambda_c^+)$ and $M_{\mathrm{BC}}(\Lambda_c^+ \pi)$ distributions. The relevant uncertainties for the signal shapes in the $M(\Lambda_c^+ \pi\pi) - M(\Lambda_c^+) + m(\Lambda_c^+)$ distributions are tested by removing the smearing Gaussian functions.

Among the above systematic variations, the most conservative ULs—i.e., the cases of $\sigma(e^+e^- \to \Lambda_c^+ \bar{\Sigma}_c^0 \pi^-)$, $\sigma(e^+e^- \to \Lambda_c^+ \bar{\Sigma}_c^{--} \pi^+)$, and $\sigma(e^+e^- \to \Lambda_c^+ \bar{\Sigma}_c^- \pi^0)$ being in a ratio of 1:1:2—are selected as the final results.

D. Final results

The upper limits on the Born cross section considering all systematic uncertainties are obtained from the likelihood distribution $\mathcal{L}(\sigma_{\mathrm{Born}}^{\mathrm{smear}})$, which is defined as

$$\mathcal{L}(\sigma_{\mathrm{Born}}^{\mathrm{smear}}) = \int \mathcal{L}(\bar{\sigma}_{\mathrm{Born}}) \exp\left(-\frac{(\sigma_{\mathrm{Born}} - \bar{\sigma}_{\mathrm{Born}})^2}{2\Delta(\sigma_{\mathrm{Born}})^2}\right) d\sigma_{\mathrm{Born}}.$$

(5)

Here, $\bar{\sigma}_{\mathrm{Born}}$ represents the Born cross section, which accounts for the additive systematic uncertainty and includes a correction to adjust the mean value based on the results of the I/O check; $\Delta(\sigma_{\mathrm{Born}})$ denotes the total multiplicative uncertainty of the Born cross section, and $\sigma_{\mathrm{Born}}^{\mathrm{smear}}$ is the Born cross section considering all systematic uncertainties. Figure 4 illustrates all the likelihood distributions. The upper limits on the Born cross sections for each of $e^+e^- \to \Sigma_c^+ \bar{\Sigma}_c^-$, $\Sigma_c^0 \bar{\Sigma}_c^0$, and $\Sigma_c^{++} \bar{\Sigma}_c^{--}$ at $\sqrt{s} = 4.918$ and 4.951 GeV are determined to be 0.96 pb and 0.74 pb, respectively, at the 90% CL.
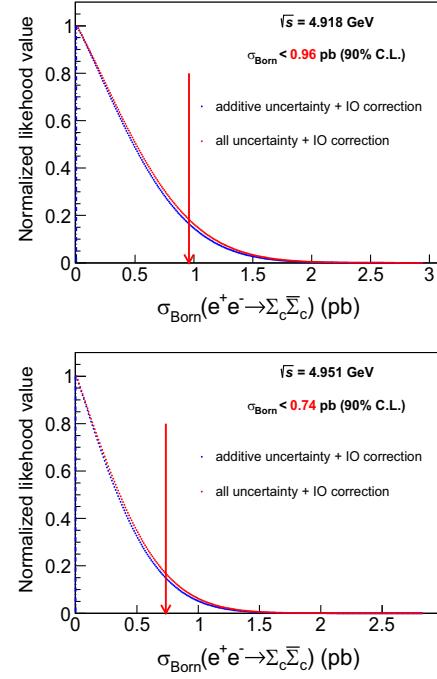
FIG. 4. Distributions of the normalized likelihoods in the positive region as functions of Born cross sections of $e^+e^- \to \Sigma_c \bar{\Sigma}_c$ at $\sqrt{s} = 4.918$ GeV (top) and $\sqrt{s} = 4.951$ GeV (bottom). The ULs at the 90% CL are determined from the positive region. The "I/O correction" refers to the adjustment of the cross section fit bias following validation through I/O checks. The blue line represents the likelihood distribution that accounts for additive systematic uncertainty and I/O correction. The red line represents the likelihood distribution that incorporates both additive and multiplicative systematic uncertainties, as well as the I/O correction.

V. MEASUREMENTS OF $e^+e^- \to \Lambda_c^+ \bar{\Sigma}_c^-$ CROSS SECTION

The "Tag Λ_c^+" method is used to measure the cross section of $e^+e^- \to \Lambda_c^+ \bar{\Sigma}_c^-$ in the energy range from 4.750 GeV to 4.951 GeV. In this analysis, the spectra of $RM(\Lambda_c^+) + M(\Lambda_c^+) - m(\Lambda_c^+)$ are studied in the range $(2.18, 2.54)$ GeV/c^2. Among all the energy points, clear $\Lambda_c^+ \bar{\Lambda}_c^-$ signals are observed, while there is no evidence of $\Lambda_c^+ \bar{\Sigma}_c^-$ signals, as shown in Fig. 5. Hence, to determine the ULs of the cross sections of $\Lambda_c^+ \bar{\Sigma}_c^-$ at each energy point, an unbinned simultaneous fit to the $RM(\Lambda_c^+) + M(\Lambda_c^+) - m(\Lambda_c^+)$ distributions in data is performed. Here, the cross section ratio $R(\sigma)$, which represents the ratio between the Born cross section of $e^+e^- \to \Lambda_c^+ \bar{\Sigma}_c^-$ and that of $e^+e^- \to \Lambda_c^+ \bar{\Lambda}_c^-$, is taken as the fitting parameter. In the fit, $e^+e^- \to \Lambda_c^+ \bar{\Sigma}_c^-$ and $e^+e^- \to \Lambda_c^+ \bar{\Lambda}_c^-$ signal shapes are obtained from MC simulations convolved with the same Gaussian function, whose parameters are left free.
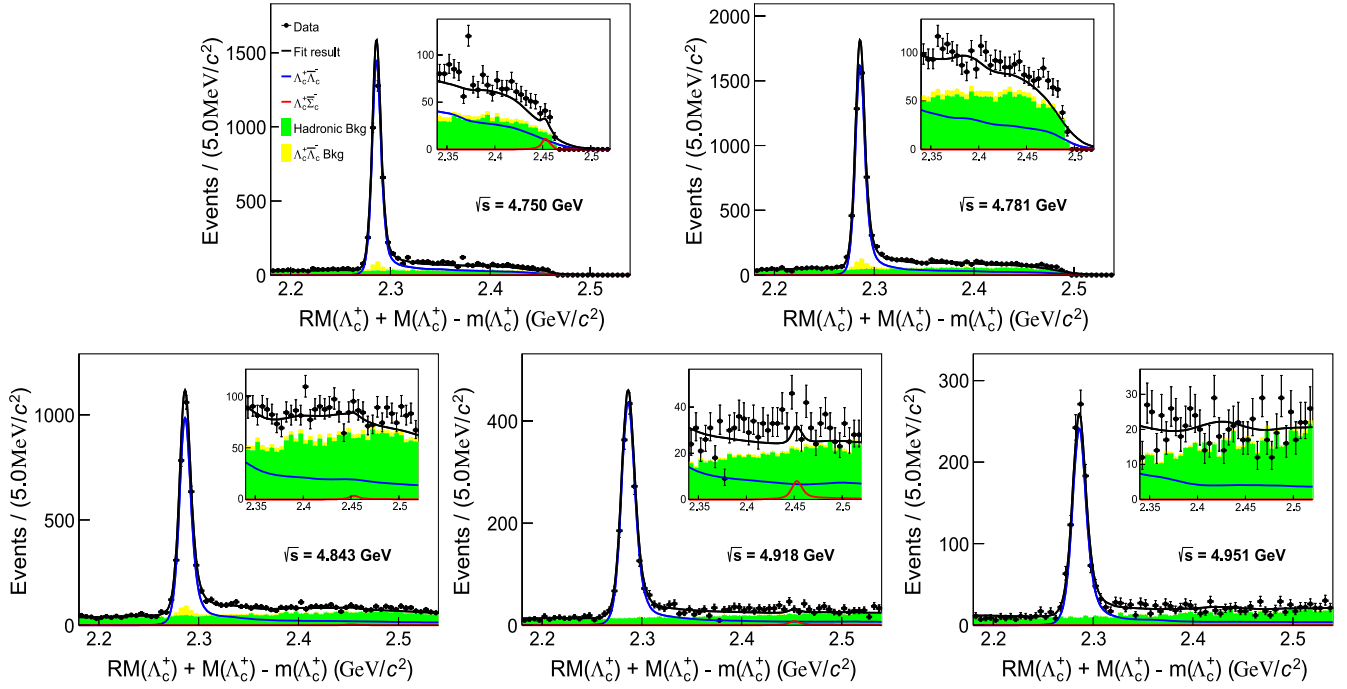
FIG. 5. Simultaneous fit to the $RM(\Lambda_c^+) + M(\Lambda_c^+) - m(\Lambda_c^+)$ distributions from 2.18 to 2.54 GeV/c^2 in data at $\sqrt{s} = 4.750$, 4.781, 4.843, 4.918, and 4.951 GeV. The small plots display the fit results in the range from 2.35 to 2.54 GeV/c^2. The dots with error bars are the experimental data, while the black curves represent the total fit functions. "Bkg" stands for the background.

Based on the studies of $e^+e^- \rightarrow \Lambda_c^+\bar{\Lambda}_c^-$ and inclusive hadronic MC samples, no peaking background is observed within the Σ_c^+ signal region. In the fit, the $\Lambda_c^+\bar{\Lambda}_c^-$ nontagged background and hadronic background are modeled using MC simulation. The yields of $\Lambda_c^+\bar{\Lambda}_c^-$ nontagged models are fixed, while the contributions of hadronic backgrounds are allowed to vary. However, the contribution of the isospin-violating three-body process $e^+e^- \rightarrow \Lambda_c^+\bar{\Lambda}_c^-\pi^0$ remains a potential factor that could influence the signal yield, and therefore is considered as a source of systematic uncertainty.

The fit results corresponding to the maximum likelihood values at $\sqrt{s} = 4.750$, 4.781, 4.843, 4.918, and 4.951 GeV are presented in Fig. 5. Following the same likelihood scan method discussed at Sec. IV B, the ULs on $R(\sigma)$ at the 90% CL are obtained.

With regard to systematic uncertainties, only additive uncertainties are considered, since the multiplicative uncertainties are naturally eliminated in $R(\sigma)$. The sources of additive uncertainties include the input line shape of $e^+e^- \rightarrow \Lambda_c^+\bar{\Sigma}_c^-$ and the contribution of $e^+e^- \rightarrow \Lambda_c^+\bar{\Lambda}_c^-\pi^0$. Considering the line shape of the input cross section of $e^+e^- \rightarrow \Lambda_c^+\bar{\Lambda}_c^-$, the uncertainty is investigated by replacing it with a plateau characterized by $\sigma \propto \frac{1}{\sqrt{s}}$. The possible contribution of $\Lambda_c^+\bar{\Lambda}_c^-\pi^0$ is considered by incorporating it into the fit model additionally. Its shape is extracted from the corresponding MC sample, with the yield being free. Among the above systematic variations, the most conservative ULs are taken as the final results, which are given in Table IV.

Concerning the Born cross section $\sigma_{\text{Born}}(e^+e^- \rightarrow \Lambda_c^+\bar{\Sigma}_c^-)$, the likelihood function is further smeared according to Eq. (5) with the input uncertainty of the Born cross section $\sigma_{\text{Born}}(e^+e^- \rightarrow \Lambda_c^+\bar{\Lambda}_c^-)$, which is studied by BESIII [19]. The likelihood ratio distribution at $\sqrt{s} = 4.750$ GeV is illustrated in Fig. 6, and the numerical results of all data samples are summarized in Table IV.

TABLE IV. Summary of the upper limits on Born cross sections of $e^+e^- \rightarrow \Lambda_c^+\bar{\Sigma}_c^-$ at 90% CL. The results of $\sigma_{\text{Born}}(e^+e^- \rightarrow \Lambda_c^+\bar{\Lambda}_c^-)$ are input from Ref. [19], where the first uncertainty represents statistical uncertainty, and the second one represents systematic uncertainty.

$\sqrt{s}$	4.750 GeV	4.781 GeV	4.843 GeV	4.918 GeV	4.951 GeV
$R(\sigma)$ (%)	<1.1	<0.6	<1.5	<3.4	<1.6
$\sigma_{\text{Born}}(e^+e^- \rightarrow \Lambda_c^+\bar{\Lambda}_c^-)$ (pb)	$134 \pm 3 \pm 4$	$127 \pm 2 \pm 4$	$83 \pm 2 \pm 3$	$96 \pm 3 \pm 4$	$88 \pm 4 \pm 3$
$\sigma_{\text{Born}}(e^+e^- \rightarrow \Lambda_c^+\bar{\Sigma}_c^-)$ (pb)	<1.52	<0.76	<1.26	<3.26	<1.38
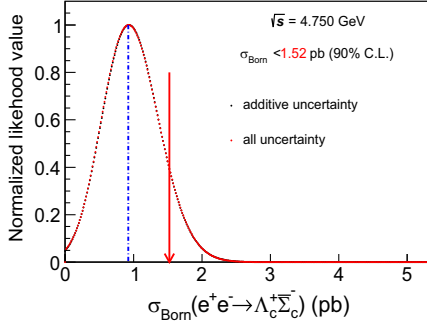
FIG. 6. Distribution of the normalized likelihood in the positive region as a function of the Born cross section of $e^+e^- \to \Lambda_c^+ \bar{\Sigma}_c^-$ at $\sqrt{s} = 4.750$ GeV. The black line represents the original likelihood distribution, while the red line represents the distribution considering all uncertainties in the $e^+e^- \to \Lambda_c^+ \bar{\Lambda}_c^-$ cross section measurement [19].

VI. SUMMARY

Using the data collected with the BESIII detectors, the measurement of the Born cross section of $e^+e^- \to \Sigma_c \bar{\Sigma}_c$ ($\Sigma_c^+ \bar{\Sigma}_c^-$, $\Sigma_c^0 \bar{\Sigma}_c^0$ and $\Sigma_c^{++} \bar{\Sigma}_c^{--}$) at $\sqrt{s} = 4.918$ and 4.951 GeV is conducted, no significant signals are observed. The upper limits at the 90% confidence level on the Born cross section are estimated to be 0.96 pb and 0.74 pb under the Hypothesis 2 line shape presented in Fig. 3, respectively.

A comparison between the cross section of $e^+e^- \to \Sigma_c \bar{\Sigma}_c$ and that of $e^+e^- \to \Lambda_c^+ \bar{\Lambda}_c^-$ near threshold (~ 250 pb) [18] reveals a suppression of at least 2 orders of magnitude in the $\Sigma_c \bar{\Sigma}_c$ cross section. This suppression might be attributed to the mass difference between "good" and "bad" diquarks, though it remains unclear whether such a mass difference alone can account for the observed effect.

A similar suppression is observed in measurements by the Belle Collaboration at 10.58 GeV for the inclusive processes $e^+e^- \to \Lambda_c^+ X$ and $e^+e^- \to \Sigma_c^0 X$, where the cross sections differ by about 2 orders of magnitude (141.79 pb vs 7.963 pb) [56]. While this aligns with the trend near the threshold, it raises a new question: the cross section of $e^+e^- \to \Sigma_c \bar{\Sigma}_c$ far from the threshold is roughly 10 times larger than the upper limit value near the threshold, calling for further investigation.

In contrast, such cross section suppression is not observed in hyperon pair production. For example, the cross sections for $e^+e^- \to \Lambda \bar{\Lambda}$ pairs (~ 300 pb) [9] and $e^+e^- \to \Sigma^0 \bar{\Sigma}^0$ pairs (~ 30 pb) [15] near 2.3 GeV differ by only an order of magnitude, indicating a distinct production mechanism compared to charmed baryons. The different behavior in hyperon production and charmed baryon productions implies the presence of certain mechanisms that have yet to be fully understood.

Regarding the process $e^+e^- \to \Lambda_c^+ \bar{\Sigma}_c^-$, the upper limit on Born cross sections at $\sqrt{s} = 4.750$, 4.781, 4.843, 4.918 and 4.951 GeV at the 90% confidence level are reported, which are about 1% relative to the Born cross sections of

$e^+e^- \to \Lambda_c^+ \bar{\Lambda}_c^-$. Despite the statistical constraints, this result is valuable in understanding the magnitude of electromagnetic process in the production of charmed baryons.

Due to limited statistics, no signals of $e^+e^- \to \Sigma_c \bar{\Sigma}_c$ or $e^+e^- \to \Lambda_c^+ \bar{\Sigma}_c^-$ have been observed. In coming years, improved measurements are expected in the upgrade of the current BEPCII [57], which would have threefold instant luminosity, and the future super τ-charm facility [58] will greatly advance the studies.

DATA AVAILABILITY

The data that support the findings of this article are not publicly available upon publication because it is not technically feasible and/or the cost of preparing, depositing, and hosting the data would be prohibitive within the terms of this research project. The data are available from the authors upon reasonable request.

[1] S. Capstick and N. Isgur, Baryons in a relativized quark model with chromodynamics, Phys. Rev. D **34,** 2809 (1986).

[2] R. Pohl *et al.*, The size of the proton, Nature (London) **466,** 213 (2010).

[3] N. Cabibbo and R. Gatto, Electron-positron colliding beam experiments, Phys. Rev. **124,** 1577 (1961).

[4] R. Baldini Ferroli and S. Pacetti, Baryon form factors at threshold, Nucl. Phys. B, Proc. Suppl. **225–227,** 211 (2012).

[5] J. P. Lees *et al.* (*BABAR* Collaboration), Measurement of the $e^+e^- \to p\bar{p}$ cross section in the energy range from 3.0 to 6.5 GeV, Phys. Rev. D **88,** 072009 (2013).

[6] R. R. Akhmetshin *et al.* (CMD-3 Collaboration), Observation of a fine structure in $e^+e^- \to$ hadrons production at the nucleon-antinucleon threshold, Phys. Lett. B **794,** 64 (2019).

[7] M. Ablikim *et al.* (BESIII Collaboration), Measurement of proton electromagnetic form factors in $e^+e^- \to p\bar{p}$ in the energy region 2.00–3.08 GeV, Phys. Rev. Lett. **124,** 042001 (2020).

[8] B. Aubert *et al.* (*BABAR* Collaboration), Study of $e^+e^- \to \Lambda\bar{\Lambda}, \Lambda\bar{\Sigma}^0, \Sigma^0\bar{\Sigma}^0$ using initial state radiation with *BABAR*, Phys. Rev. D **76,** 092006 (2007).

[9] M. Ablikim *et al.* (BESIII Collaboration), Observation of a cross-section enhancement near mass threshold in $e^+e^- \to \Lambda\bar{\Lambda}$, Phys. Rev. D **97,** 032013 (2018).

[10] M. Ablikim *et al.* (BESIII Collaboration), Oscillating features in the electromagnetic structure of the neutron, Nat. Phys. **17,** 1200 (2021).

[11] M. N. Achasov *et al.* (SND Collaboration), Experimental study of the $e^+e^- \to n\bar{n}$ process at the VEPP-2000 e^+e^- collider with the SND detector, Eur. Phys. J. C **82,** 761 (2022).

[12] M. N. Achasov *et al.* (SND Collaboration), Measuring the neutron timelike electromagnetic form factor with the SND detector, Phys. At. Nucl. **86,** 1165 (2023).

[13] M. N. Achasov *et al.*, Cross section of the process $e^+e^- \to n\bar{n}$ near the threshold, Phys. At. Nucl. **87,** 604 (2024).

[14] M. Ablikim *et al.* (BESIII Collaboration), Measurements of Σ^+ and Σ^- time-like electromagnetic form factors for center-of-mass energies from 2.3864 to 3.0200 GeV, Phys. Lett. B **814,** 136110 (2021).

[15] M. Ablikim *et al.* (BESIII Collaboration), Measurement of the $e^+e^- \to \Sigma^0\bar{\Sigma}^0$ cross sections at center-of-mass energies from 2.3864 to 3.0200 GeV, Phys. Lett. B **831,** 137187 (2022).

[16] M. Ablikim *et al.* (BESIII Collaboration), Measurement of the $e^+e^- \to \Lambda\bar{\Sigma}^0$ + c.c. cross sections at $\sqrt{s}$ from 2.3094 to 3.0800 GeV, Phys. Rev. D **109,** 012002 (2024).

[17] G. Pakhlova *et al.* (Belle Collaboration), Observation of a near-threshold enhancement in the $e^+e^- \to \Lambda_c^+\bar{\Lambda}_c^-$ cross section using initial-state radiation, Phys. Rev. Lett. **101,** 172001 (2008).

[18] M. Ablikim *et al.* (BESIII Collaboration), Precision measurement of the $e^+e^- \to \Lambda_c^+\bar{\Lambda}_c^-$ cross section near threshold, Phys. Rev. Lett. **120,** 132001 (2018).

[19] M. Ablikim *et al.* (BESIII Collaboration), Measurement of energy-dependent pair-production cross section and electromagnetic form factors of a charmed baryon, Phys. Rev. Lett. **131,** 191901 (2023).

[20] J. Yelton *et al.* (Belle Collaboration), Measurement of the masses and widths of the $\Sigma_c(2455)^+$ and $\Sigma_c(2520)^+$ baryons, Phys. Rev. D **104,** 052003 (2021).

[21] S. H. Lee *et al.* (Belle Collaboration), Measurements of the masses and widths of the $\Sigma_c(2455)^{0/++}$ and $\Sigma_c(2520)^{0/++}$ baryons, Phys. Rev. D **89,** 091102 (2014).

[22] R. L. Jaffe, Exotica, Phys. Rep. **409,** 1 (2005).

[23] W. Meguro, Y.-R. Liu, and M. Oka, Possible $\Lambda_c\Lambda_c$ molecular bound state, Phys. Lett. B **704,** 547 (2011).

[24] N. Lee, Z.-G. Luo, X.-L. Chen, and S.-L. Zhu, Possible deuteron-like molecular states composed of heavy baryons, Phys. Rev. D **84,** 014031 (2011).

[25] N. Li and S.-L. Zhu, Hadronic molecular states composed of heavy flavor baryons, Phys. Rev. D **86,** 014020 (2012).

[26] X.-K. Dong, F.-K. Guo, and B.-S. Zou, A survey of heavy–heavy hadronic molecules, Commun. Theor. Phys. **73,** 125201 (2021).

[27] E. Epelbaum, H.-W. Hammer, and U.-G. Meissner, Modern theory of nuclear forces, Rev. Mod. Phys. **81,** 1773 (2009).

[28] K. Chen, B.-L. Huang, B. Wang, and S.-L. Zhu, $\Sigma_c\Sigma_c$ interactions in chiral effective field theory, arXiv:2204 .13316.

[29] A. Valcarce, H. Garcilazo, F. Fernandez, and P. Gonzalez, Quark-model study of few-baryon systems, Rep. Prog. Phys. **68,** 965 (2005).

[30] Z. Xia, S. Fan, X. Zhu, H. Huang, and J. Ping, Search for doubly heavy dibaryons in the quark delocalization color screening model, Phys. Rev. C **105,** 025201 (2022).

[31] T. Iritani *et al.* (HAL QCD Collaboration), $N\Omega$ dibaryon from lattice QCD near the physical point, Phys. Lett. B **792,** 284 (2019).

[32] S. M. Gerasyuta and E. E. Matskevich, Dibaryons with two heavy quarks, Int. J. Mod. Phys. E **21,** 1250058 (2012).

[33] M. Ablikim *et al.* (BESIII Collaboration), Luminosities and energies of e^+ e^- collision data taken between = 4.61 GeV and 4.95 GeV at BESIII, Chin. Phys. C **46,** 113003 (2022).

[34] M. Ablikim *et al.* (BESIII Collaboration), Measurements of Born cross sections for $e^+e^- \to \Lambda_c^+\bar{\Lambda}_c(2595)^-$ + c.c. and $e^+e^- \to \Lambda_c^+\bar{\Lambda}_c(2625)^-$ + c.c. at $\sqrt{s} = 4.918.0$ and 4.950.9 MeV, Phys. Rev. D **109,** L071104 (2024).

[35] R. L. Workman *et al.* (Particle Data Group), Review of particle physics, Prog. Theor. Exp. Phys. **2022,** 083C01 (2022).

[36] H.-B. Li and X.-R. Lyu, Study of the standard model with weak decays of charmed hadrons at BESIII, Natl. Sci. Rev. **8,** nwab181 (2021).

[37] M. Ablikim *et al.* (BESIII Collaboration), Design and construction of the BESIII detector, Nucl. Instrum. Methods Phys. Res., Sect. A **614,** 345 (2010).

[38] C. Yu *et al.*, BEPCII performance and beam dynamics studies on luminosity, in *Proceedings of the 7th International Particle Accelerator Conference* (2016), p. TUYA01.

[39] S. Agostinelli *et al.* (GEANT4 Collaboration), GEANT4: A simulation toolkit, Nucl. Instrum. Methods Phys. Res., Sect. A **506,** 250 (2003).

[40] S. Jadach, B. F. L. Ward, and Z. Was, Coherent exclusive exponentiation for precision Monte Carlo calculations, Nucl. Phys. B, Proc. Suppl. **89,** 106 (2000).

[41] S. Jadach, B. F. L. Ward, and Z. Was, The precision Monte Carlo event generator K K for two fermion final

states in $e^+ e^-$ collisions, Comput. Phys. Commun. **130,** 260 (2000).

[42] R.-G. Ping, Event generators at BESIII, Chin. Phys. C **32,** 599 (2008).

[43] D. J. Lange, The EvtGen particle decay simulation package, Nucl. Instrum. Methods Phys. Res., Sect. A **462,** 152 (2001).

[44] J. C. Chen, G. S. Huang, X. R. Qi, D. H. Zhang, and Y. S. Zhu, Event generator for J/ψ and $\psi(2S)$ decay, Phys. Rev. D **62,** 034003 (2000).

[45] R.-L. Yang, R.-G. Ping, and H. Chen, Tuning and validation of the Lundcharm model with J/ψ decays, Chin. Phys. Lett. **31,** 061301 (2014).

[46] E. Richter-Was, QED bremsstrahlung in semileptonic B and leptonic tau decays, Phys. Lett. B **303,** 163 (1993).

[47] M. Ablikim *et al.* (BESIII Collaboration), Measurement of singly cabibbo suppressed decays $\Lambda_c^+ \to p\pi^+\pi^-$ and $\Lambda_c^+ \to pK^+K^-$, Phys. Rev. Lett. **117,** 232002 (2016); **120,** 029903(A) (2018).

[48] P.-R. Li, X.-R. Lyu, and Y. Zheng, Experimental overview on the charmed baryon decays, (2025).

[49] M. Ablikim *et al.* (BESIII Collaboration), The production and decay dynamics of the charmed baryon Λ_c^+ in e^+e^- annihilations near threshold, arXiv:2508.11400.

[50] D. Wang *et al.* (Belle Collaboration), Measurement of the mass and width of the $\Lambda_c(2625)^+$ charmed baryon and the branching ratios of $\Lambda_c(2625)^+ \to \Sigma_c^0\pi^+$ and $\Lambda_c(2625)^+ \to \Sigma_c^{++}\pi^-$, Phys. Rev. D **107,** 032008 (2023).

[51] S. Actis *et al.* (Working Group on Radiative Corrections, Monte Carlo Generators for Low Energies), Quest for precision in hadronic cross sections at low energy: Monte Carlo tools vs. experimental data, Eur. Phys. J. C **66,** 585 (2010).

[52] S. Jadach, B. F. L. Ward, and Z. Was, Coherent exclusive exponentiation for precision Monte Carlo calculations, Phys. Rev. D **63,** 113009 (2001).

[53] M. Ablikim *et al.* (BESIII Collaboration), Measurements of absolute hadronic branching fractions of Λ_c^+ baryon, Phys. Rev. Lett. **116,** 052001 (2016).

[54] R.-G. Ping *et al.*, Tuning and validation of hadronic event generator for R value measurements in the tau-charm region, Chin. Phys. C **40,** 113002 (2016).

[55] D. Liu, W. Wang, R. B. Ferroli, and G. Huang, Two methods for the determination of beam energy spread near $\Lambda_c^+\bar{\Lambda}_c^-$ production threshold, J. Instrum. **13,** P12017 (2018).

[56] M. Niiyama *et al.* (Belle Collaboration), Production cross sections of hyperons and charmed baryons from e^+e^- annihilation near $\sqrt{s} = 10.52$ GeV, Phys. Rev. D **97,** 072005 (2018).

[57] H. Geng, J. Xing, C. Yu, and Y. Zhang, An alternative design for BEPCII upgrade, JACoW **IPAC2022,** WEOXGD3 (2022).

[58] M. Achasov *et al.*, STCF conceptual design report (Volume 1): Physics & detector, Front. Phys. (Beijing) **19,** 14701 (2024).

[59] https://cstr.cn/31109.02.BEPC.

M. Ablikim,[1] M. N. Achasov,[4,b] P. Adlarson,[77] X. C. Ai,[82] R. Aliberti,[36] A. Amoroso,[76a,76c] Q. An,[73,59,†] Y. Bai,[58] O. Bakina,[37] Y. Ban,[47,g] H.-R. Bao,[65] V. Batozskaya,[1,45] K. Begzsuren,[33] N. Berger,[36] M. Berlowski,[45] M. Bertani,[29a] D. Bettoni,[30a] F. Bianchi,[76a,76c] E. Bianco,[76a,76c] A. Bortone,[76a,76c] I. Boyko,[37] R. A. Briere,[5] A. Brueggemann,[70] H. Cai,[78] M. H. Cai,[39,j,k] X. Cai,[1,59] A. Calcaterra,[29a] G. F. Cao,[1,65] N. Cao,[1,65] S. A. Cetin,[63a] X. Y. Chai,[47,g] J. F. Chang,[1,59] G. R. Che,[44] Y. Z. Che,[1,59,65] G. Chelkov,[37,a] C. H. Chen,[9] Chao Chen,[56] G. Chen,[1] H. S. Chen,[1,65] H. Y. Chen,[21] M. L. Chen,[1,59,65] S. J. Chen,[43] S. L. Chen,[46] S. M. Chen,[62] T. Chen,[1,65] X. R. Chen,[32,65] X. T. Chen,[1,65] X. Y. Chen,[12,f] Y. B. Chen,[1,59] Y. Q. Chen,[35] Y. Q. Chen,[16] Z. J. Chen,[26,h] Z. K. Chen,[60] S. K. Choi,[10] X. Chu,[12,f] G. Cibinetto,[30a] F. Cossio,[76c] J. Cottee-Meldrum,[64] J. J. Cui,[51] H. L. Dai,[1,59] J. P. Dai,[80] A. Dbeyssi,[19] R. E. de Boer,[3] D. Dedovich,[37] C. Q. Deng,[74] Z. Y. Deng,[1] A. Denig,[36] I. Denysenko,[37] M. Destefanis,[76a,76c] F. De Mori,[76a,76c] B. Ding,[68,1] X. X. Ding,[47,g] Y. Ding,[41] Y. Ding,[35] Y. X. Ding,[31] J. Dong,[1,59] L. Y. Dong,[1,65] M. Y. Dong,[1,59,65] X. Dong,[78] M. C. Du,[1] S. X. Du,[82] S. X. Du,[12,f] Y. Y. Duan,[56] Z. H. Duan,[43] P. Egorov,[37,a] G. F. Fan,[43] J. J. Fan,[20] Y. H. Fan,[46] J. Fang,[1,59] J. Fang,[60] S. S. Fang,[1,65] W. X. Fang,[1] Y. Q. Fang,[1,59] R. Farinelli,[30a] L. Fava,[76b,76c] F. Feldbauer,[3] G. Felici,[29a] C. Q. Feng,[73,59] J. H. Feng,[16] L. Feng,[39,j,k] Q. X. Feng,[39,j,k] Y. T. Feng,[73,59] M. Fritsch,[3] C. D. Fu,[1] J. L. Fu,[65] Y. W. Fu,[1,65] H. Gao,[65] X. B. Gao,[42] Y. Gao,[73,59] Y. N. Gao,[47,g] Y. N. Gao,[20] Y. Y. Gao,[31] S. Garbolino,[76c] I. Garzia,[30a,30b] P. T. Ge,[20] Z. W. Ge,[43] C. Geng,[60] E. M. Gersabeck,[69] A. Gilman,[71] K. Goetzen,[13] J. D. Gong,[35] L. Gong,[41] W. X. Gong,[1,59] W. Gradl,[36] S. Gramigna,[30a,30b] M. Greco,[76a,76c] M. H. Gu,[1,59] Y. T. Gu,[15] C. Y. Guan,[1,65] A. Q. Guo,[32] L. B. Guo,[42] M. J. Guo,[51] R. P. Guo,[50] Y. P. Guo,[12,f] A. Guskov,[37,a] J. Gutierrez,[28] K. L. Han,[65] T. T. Han,[1] F. Hanisch,[3] K. D. Hao,[73,59] X. Q. Hao,[20] F. A. Harris,[67] K. K. He,[56] K. L. He,[1,65] F. H. Heinsius,[3] C. H. Heinz,[36] Y. K. Heng,[1,59,65] C. Herold,[61] T. Holtmann,[3] P. C. Hong,[35] G. Y. Hou,[1,65] X. T. Hou,[1,65] Y. R. Hou,[65] Z. L. Hou,[1] H. M. Hu,[1,65] J. F. Hu,[57,i] Q. P. Hu,[73,59] S. L. Hu,[12,f] T. Hu,[1,59,65] Y. Hu,[1] Z. M. Hu,[60] G. S. Huang,[73,59] K. X. Huang,[60] L. Q. Huang,[32,65] P. Huang,[43] X. T. Huang,[51] Y. P. Huang,[1] Y. S. Huang,[60] T. Hussain,[75] N. Hüsken,[36] N. in der Wiesche,[70] J. Jackson,[28] S. Janchiv,[33] Q. Ji,[1] Q. P. Ji,[20] W. Ji,[1,65] X. B. Ji,[1,65] X. L. Ji,[1,59] Y. Y. Ji,[51] Z. K. Jia,[73,59] D. Jiang,[1,65] H. B. Jiang,[78] P. C. Jiang,[47,g] S. J. Jiang,[9] T. J. Jiang,[17] X. S. Jiang,[1,59,65] Y. Jiang,[65] J. B. Jiao,[51] J. K. Jiao,[35] Z. Jiao,[24] S. Jin,[43] Y. Jin,[68] M. Q. Jing,[1,65] X. M. Jing,[65] T. Johansson,[77]

S. Kabana,[34] N. Kalantar-Nayestanaki,[66] X. L. Kang,[9] X. S. Kang,[41] M. Kavatsyuk,[66] B. C. Ke,[82] V. Khachatryan,[28] A. Khoukaz,[70] R. Kiuchi,[1] O. B. Kolcu,[63a] B. Kopf,[3] M. Kuessner,[3] X. Kui,[1,65] N. Kumar,[27] A. Kupsc,[45,77] W. Kühn,[38] Q. Lan,[74] W. N. Lan,[20] T. T. Lei,[73,59] M. Lellmann,[36] T. Lenz,[36] C. Li,[73,59] C. Li,[48] C. Li,[44] C. H. Li,[40] C. K. Li,[21] D. M. Li,[82] F. Li,[1,59] G. Li,[1] H. B. Li,[1,65] H. J. Li,[20] H. N. Li,[57,i] Hui Li,[44] J. R. Li,[62] J. S. Li,[60] K. Li,[1] K. L. Li,[20] K. L. Li,[39,j,k] L. J. Li,[1,65] Lei Li,[49] M. H. Li,[44] M. R. Li,[1,65] P. L. Li,[65] P. R. Li,[39,j,k] Q. M. Li,[1,65] Q. X. Li,[51] R. Li,[18,32] S. X. Li,[12] T. Li,[51] T. Y. Li,[44] W. D. Li,[1,65] W. G. Li,[1,†] X. Li,[1,65] X. H. Li,[73,59] X. L. Li,[51] X. Y. Li,[1,8] X. Z. Li,[60] Y. Li,[20] Y. G. Li,[47,g] Y. P. Li,[35] Z. J. Li,[60] Z. Y. Li,[80] C. Liang,[43] H. Liang,[73,59] Y. F. Liang,[55] Y. T. Liang,[32,65] G. R. Liao,[14] L. B. Liao,[60] M. H. Liao,[60] Y. P. Liao,[1,65] J. Libby,[27] A. Limphirat,[61] C. C. Lin,[56] C. X. Lin,[65] D. X. Lin,[32,65] L. Q. Lin,[40] T. Lin,[1] B. J. Liu,[1] B. X. Liu,[78] C. Liu,[35] C. X. Liu,[1] F. Liu,[1] F. H. Liu,[54] Feng Liu,[6] G. M. Liu,[57,i] H. Liu,[39,j,k] H. B. Liu,[15] H. H. Liu,[1] H. M. Liu,[1,65] Huihui Liu,[22] J. B. Liu,[73,59] J. J. Liu,[21] K. Liu,[39,j,k] K. Liu,[74] K. Y. Liu,[41] Ke Liu,[23] L. Liu,[73,59] L. C. Liu,[44] Lu Liu,[44] M. H. Liu,[12,f] P. L. Liu,[1] Q. Liu,[65] S. B. Liu,[73,59] T. Liu,[12,f] W. K. Liu,[44] W. M. Liu,[73,59] W. T. Liu,[40] X. Liu,[39,j,k] X. Liu,[40] X. K. Liu,[39,j,k] X. Y. Liu,[78] Y. Liu,[39,j,k] Y. Liu,[82] Yuan Liu,[82] Y. B. Liu,[44] Z. A. Liu,[1,59,65] Z. D. Liu,[9] Z. Q. Liu,[51] X. C. Lou,[1,59,65] F. X. Lu,[60] H. J. Lu,[24] J. G. Lu,[1,59] X. L. Lu,[16] Y. Lu,[7] Y. H. Lu,[1,65] Y. P. Lu,[1,59] Z. H. Lu,[1,65] C. L. Luo,[42] J. R. Luo,[60] J. S. Luo,[1,65] M. X. Luo,[81] T. Luo,[12,f] X. L. Luo,[1,59] Z. Y. Lv,[23] X. R. Lyu,[65,o] Y. F. Lyu,[44] Y. H. Lyu,[82] F. C. Ma,[41] H. Ma,[80] H. L. Ma,[1] J. L. Ma,[1,65] L. L. Ma,[51] L. R. Ma,[68] Q. M. Ma,[1] R. Q. Ma,[1,65] R. Y. Ma,[20] T. Ma,[73,59] X. T. Ma,[1,65] X. Y. Ma,[1,59] Y. M. Ma,[32] F. E. Maas,[19] I. MacKay,[71] M. Maggiora,[76a,76c] S. Malde,[71] H. X. Mao,[39,j,k] Y. J. Mao,[47,g] Z. P. Mao,[1] S. Marcello,[76a,76c] A. Marshall,[64] F. M. Melendi,[30a,30b] Y. H. Meng,[65] Z. X. Meng,[68] J. G. Messchendorp,[13,66] G. Mezzadri,[30a] H. Miao,[1,65] T. J. Min,[43] R. E. Mitchell,[28] X. H. Mo,[1,59,65] B. Moses,[28] N. Yu. Muchnoi,[4,b] J. Muskalla,[36] Y. Nefedov,[37] F. Nerling,[19,d] L. S. Nie,[21] I. B. Nikolaev,[4,b] Z. Ning,[1,59] S. Nisar,[11,l] Q. L. Niu,[39,j,k] W. D. Niu,[12,f] C. Normand,[64] S. L. Olsen,[10,65] Q. Ouyang,[1,59,65] S. Pacetti,[29b,29c] X. Pan,[56] Y. Pan,[58] A. Pathak,[10] Y. P. Pei,[73,59] M. Pelizaeus,[3] H. P. Peng,[73,59] X. J. Peng,[39,j,k] Y. Y. Peng,[39,j,k] K. Peters,[13,d] K. Petridis,[64] J. L. Ping,[42] R. G. Ping,[1,65] S. Plura,[36] V. Prasad,[34] F. Z. Qi,[1] H. R. Qi,[62] M. Qi,[43] S. Qian,[1,59] W. B. Qian,[65] C. F. Qiao,[65] J. H. Qiao,[20] J. J. Qin,[74] J. L. Qin,[56] L. Q. Qin,[14] L. Y. Qin,[73,59] P. B. Qin,[74] X. P. Qin,[12,f] X. S. Qin,[51] Z. H. Qin,[1,59] J. F. Qiu,[1] Z. H. Qu,[74] J. Rademacker,[64] C. F. Redmer,[36] A. Rivetti,[76c] M. Rolo,[76c] G. Rong,[1,65] S. S. Rong,[1,65] F. Rosini,[29b,29c] Ch. Rosner,[19] M. Q. Ruan,[1,59] N. Salone,[45] A. Sarantsev,[37,c] Y. Schelhaas,[36] K. Schoenning,[77] M. Scodeggio,[30a] K. Y. Shan,[12,f] W. Shan,[25] X. Y. Shan,[73,59] Z. J. Shang,[39,j,k] J. F. Shangguan,[17] L. G. Shao,[1,65] M. Shao,[73,59] C. P. Shen,[12,f] H. F. Shen,[1,8] W. H. Shen,[65] X. Y. Shen,[1,65] B. A. Shi,[65] H. Shi,[73,59] J. L. Shi,[12,f] J. Y. Shi,[1] S. Y. Shi,[74] X. Shi,[1,59] H. L. Song,[73,59] J. J. Song,[20] T. Z. Song,[60] W. M. Song,[35] Y. J. Song,[12,f] Y. X. Song,[47,g,m] S. Sosio,[76a,76c] S. Spataro,[76a,76c] F. Stieler,[36] S. S. Su,[41] Y. J. Su,[65] G. B. Sun,[78] G. X. Sun,[1] H. Sun,[65] H. K. Sun,[1] J. F. Sun,[20] K. Sun,[62] L. Sun,[78] S. S. Sun,[1,65] T. Sun,[52,e] Y. C. Sun,[78] Y. H. Sun,[31] Y. J. Sun,[73,59] Y. Z. Sun,[1] Z. Q. Sun,[1,65] Z. T. Sun,[51] C. J. Tang,[55] G. Y. Tang,[1] J. Tang,[60] J. J. Tang,[73,59] L. F. Tang,[40] Y. A. Tang,[78] L. Y. Tao,[74] M. Tat,[71] J. X. Teng,[73,59] J. Y. Tian,[73,59] W. H. Tian,[60] Y. Tian,[32] Z. F. Tian,[78] I. Uman,[63b] B. Wang,[1] B. Wang,[60] Bo Wang,[73,59] C. Wang,[39,j,k] C. Wang,[20] Cong Wang,[23] D. Y. Wang,[47,g] H. J. Wang,[39,j,k] J. J. Wang,[78] K. Wang,[1,59] L. L. Wang,[1] L. W. Wang,[35] M. Wang,[51] M. Wang,[73,59] N. Y. Wang,[65] S. Wang,[12,f] T. Wang,[12,f] T. J. Wang,[44] W. Wang,[60] Wei Wang,[74] W. P. Wang,[36,73,59,n] X. Wang,[47,g] X. F. Wang,[39,j,k] X. J. Wang,[40] X. L. Wang,[12,f] X. N. Wang,[1] Y. Wang,[62] Y. D. Wang,[46] Y. F. Wang,[1,59,65] Y. H. Wang,[39,j,k] Y. J. Wang,[73,59] Y. L. Wang,[20] Y. N. Wang,[78] Y. Q. Wang,[1] Yaqian Wang,[18] Yi Wang,[62] Yuan Wang,[18,32] Z. Wang,[1,59] Z. L. Wang,[74] Z. L. Wang,[2] Z. Q. Wang,[12,f] Z. Y. Wang,[1,65] D. H. Wei,[14] H. R. Wei,[44] F. Weidner,[70] S. P. Wen,[1] Y. R. Wen,[40] U. Wiedner,[3] G. Wilkinson,[71] M. Wolke,[77] C. Wu,[40] J. F. Wu,[1,8] L. H. Wu,[1] L. J. Wu,[1,65] L. J. Wu,[20] Lianjie Wu,[20] S. G. Wu,[1,65] S. M. Wu,[65] X. Wu,[12,f] X. H. Wu,[35] Y. J. Wu,[32] Z. Wu,[1,59] L. Xia,[73,59] X. M. Xian,[40] B. H. Xiang,[1,65] D. Xiao,[39,j,k] G. Y. Xiao,[43] H. Xiao,[74] Y. L. Xiao,[12,f] Z. J. Xiao,[42] C. Xie,[43] K. J. Xie,[1,65] X. H. Xie,[47,g] Y. Xie,[51] Y. G. Xie,[1,59] Y. H. Xie,[6] Z. P. Xie,[73,59] T. Y. Xing,[1,65] C. F. Xu,[1,65] C. J. Xu,[60] G. F. Xu,[1] H. Y. Xu,[68,2] H. Y. Xu,[2] M. Xu,[73,59] Q. J. Xu,[17] Q. N. Xu,[31] T. D. Xu,[74] W. Xu,[1] W. L. Xu,[68] X. P. Xu,[56] Y. Xu,[41] Y. Xu,[12,f] Y. C. Xu,[79] Z. S. Xu,[65] F. Yan,[12,f] H. Y. Yan,[40] L. Yan,[12,f] W. B. Yan,[73,59] W. C. Yan,[82] W. H. Yan,[6] W. P. Yan,[20] X. Q. Yan,[1,65] H. J. Yang,[52,e] H. L. Yang,[35] H. X. Yang,[1] J. H. Yang,[43] R. J. Yang,[20] T. Yang,[1] Y. Yang,[12,f] Y. F. Yang,[44] Y. H. Yang,[43] Y. Q. Yang,[9] Y. X. Yang,[1,65] Y. Z. Yang,[20] M. Ye,[1,59] M. H. Ye,[8] Z. J. Ye,[57,i] Junhao Yin,[44] Z. Y. You,[60] B. X. Yu,[1,59,65] C. X. Yu,[44] G. Yu,[13] J. S. Yu,[26,h] M. C. Yu,[41] T. Yu,[74] X. D. Yu,[47,g] Y. C. Yu,[82] C. Z. Yuan,[1,65] H. Yuan,[1,65] J. Yuan,[35] J. Yuan,[46] L. Yuan,[2] S. C. Yuan,[1,65] X. Q. Yuan,[1] Y. Yuan,[1,65] Z. Y. Yuan,[60] C. X. Yue,[40] Ying Yue,[20] A. A. Zafar,[75] S. H. Zeng,[64] X. Zeng,[12,f] Y. Zeng,[26,h] Yujie Zeng,[60] Y. J. Zeng,[1,65] X. Y. Zhai,[35] Y. H. Zhan,[60] A. Q. Zhang,[1,65] B. L. Zhang,[1,65] B. X. Zhang,[1] D. H. Zhang,[44] G. Y. Zhang,[20] G. Y. Zhang,[1,65] H. Zhang,[73,59] H. Zhang,[82] H. C. Zhang,[1,59,65] H. H. Zhang,[60] H. Q. Zhang,[1,59,65] H. R. Zhang,[73,59] H. Y. Zhang,[1,59] Jin Zhang,[82] J. Zhang,[60] J. J. Zhang,[53] J. L. Zhang,[21]

J. Q. Zhang,[42] J. S. Zhang,[12,f] J. W. Zhang,[1,59,65] J. X. Zhang,[39,j,k] J. Y. Zhang,[1] J. Z. Zhang,[1,65] Jianyu Zhang,[65] L. M. Zhang,[62] Lei Zhang,[43] N. Zhang,[82] P. Zhang,[1,65] Q. Zhang,[20] Q. Y. Zhang,[35] R. Y. Zhang,[39,j,k] S. H. Zhang,[1,65] Shulei Zhang,[26,h] X. M. Zhang,[1] X. Y. Zhang,[41] X. Y. Zhang,[51] Y. Zhang,[1] Y. Zhang,[74] Y. T. Zhang,[82] Y. H. Zhang,[1,59] Y. M. Zhang,[40] Y. P. Zhang,[73,59] Z. D. Zhang,[1] Z. H. Zhang,[1] Z. L. Zhang,[35] Z. L. Zhang,[56] Z. X. Zhang,[20] Z. Y. Zhang,[78] Z. Y. Zhang,[44] Z. Z. Zhang,[46] Zh. Zh. Zhang,[20] G. Zhao,[1] J. Y. Zhao,[1,65] J. Z. Zhao,[1,59] L. Zhao,[1] L. Zhao,[73,59] M. G. Zhao,[44] N. Zhao,[80] R. P. Zhao,[65] S. J. Zhao,[82] Y. B. Zhao,[1,59] Y. L. Zhao,[56] Y. X. Zhao,[32,65] Z. G. Zhao,[73,59] A. Zhemchugov,[37,a] B. Zheng,[74] B. M. Zheng,[35] J. P. Zheng,[1,59] W. J. Zheng,[1,65] X. R. Zheng,[20] Y. H. Zheng,[65,o] B. Zhong,[42] C. Zhong,[20] H. Zhou,[36,51,n] J. Q. Zhou,[35] J. Y. Zhou,[35] S. Zhou,[6] X. Zhou,[78] X. K. Zhou,[6] X. R. Zhou,[73,59] X. Y. Zhou,[40] Y. X. Zhou,[79] Y. Z. Zhou,[12,f] A. N. Zhu,[65] J. Zhu,[44] K. Zhu,[1] K. J. Zhu,[1,59,65] K. S. Zhu,[12,f] L. Zhu,[35] L. X. Zhu,[65] S. H. Zhu,[72] T. J. Zhu,[12,f] W. D. Zhu,[42] W. D. Zhu,[12,f] W. J. Zhu,[1] W. Z. Zhu,[20] Y. C. Zhu,[73,59] Z. A. Zhu,[1,65] X. Y. Zhuang,[44] J. H. Zou,[1] and J. Zu[73,59]

(BESIII Collaboration)

[1]*Institute of High Energy Physics, Beijing 100049, People's Republic of China*
[2]*Beihang University, Beijing 100191, People's Republic of China*
[3]*Bochum Ruhr-University, D-44780 Bochum, Germany*
[4]*Budker Institute of Nuclear Physics SB RAS (BINP), Novosibirsk 630090, Russia*
[5]*Carnegie Mellon University, Pittsburgh, Pennsylvania 15213, USA*
[6]*Central China Normal University, Wuhan 430079, People's Republic of China*
[7]*Central South University, Changsha 410083, People's Republic of China*
[8]*China Center of Advanced Science and Technology, Beijing 100190, People's Republic of China*
[9]*China University of Geosciences, Wuhan 430074, People's Republic of China*
[10]*Chung-Ang University, Seoul, 06974, Republic of Korea*
[11]*COMSATS University Islamabad, Lahore Campus, Defence Road, Off Raiwind Road,*
54000 Lahore, Pakistan
[12]*Fudan University, Shanghai 200433, People's Republic of China*
[13]*GSI Helmholtzcentre for Heavy Ion Research GmbH, D-64291 Darmstadt, Germany*
[14]*Guangxi Normal University, Guilin 541004, People's Republic of China*
[15]*Guangxi University, Nanning 530004, People's Republic of China*
[16]*Guangxi University of Science and Technology, Liuzhou 545006, People's Republic of China*
[17]*Hangzhou Normal University, Hangzhou 310036, People's Republic of China*
[18]*Hebei University, Baoding 071002, People's Republic of China*
[19]*Helmholtz Institute Mainz, Staudinger Weg 18, D-55099 Mainz, Germany*
[20]*Henan Normal University, Xinxiang 453007, People's Republic of China*
[21]*Henan University, Kaifeng 475004, People's Republic of China*
[22]*Henan University of Science and Technology, Luoyang 471003, People's Republic of China*
[23]*Henan University of Technology, Zhengzhou 450001, People's Republic of China*
[24]*Huangshan College, Huangshan 245000, People's Republic of China*
[25]*Hunan Normal University, Changsha 410081, People's Republic of China*
[26]*Hunan University, Changsha 410082, People's Republic of China*
[27]*Indian Institute of Technology Madras, Chennai 600036, India*
[28]*Indiana University, Bloomington, Indiana 47405, USA*
[29a]*INFN Laboratori Nazionali di Frascati, INFN Laboratori Nazionali di Frascati, I-00044, Frascati, Italy*
[29b]*INFN Sezione di Perugia, I-06100, Perugia, Italy*
[29c]*University of Perugia, I-06100, Perugia, Italy*
[30a]*INFN Sezione di Ferrara, INFN Sezione di Ferrara, I-44122, Ferrara, Italy*
[30]*University of Ferrara, I-44122, Ferrara, Italy*
[31]*Inner Mongolia University, Hohhot 010021, People's Republic of China*
[32]*Institute of Modern Physics, Lanzhou 730000, People's Republic of China*
[33]*Institute of Physics and Technology, Mongolian Academy of Sciences, Peace Avenue 54B,*
Ulaanbaatar 13330, Mongolia
[34]*Instituto de Alta Investigación, Universidad de Tarapacá, Casilla 7D, Arica 1000000, Chile*
[35]*Jilin University, Changchun 130012, People's Republic of China*
[36]*Johannes Gutenberg University of Mainz, Johann-Joachim-Becher-Weg 45, D-55099 Mainz, Germany*
[37]*Joint Institute for Nuclear Research, 141980 Dubna, Moscow region, Russia*
[38]*Justus-Liebig-Universitaet Giessen, II. Physikalisches Institut, Heinrich-Buff-Ring 16,*
D-35392 Giessen, Germany

[39]Lanzhou University, Lanzhou 730000, People's Republic of China
[40]Liaoning Normal University, Dalian 116029, People's Republic of China
[41]Liaoning University, Shenyang 110036, People's Republic of China
[42]Nanjing Normal University, Nanjing 210023, People's Republic of China
[43]Nanjing University, Nanjing 210093, People's Republic of China
[44]Nankai University, Tianjin 300071, People's Republic of China
[45]National Centre for Nuclear Research, Warsaw 02-093, Poland
[46]North China Electric Power University, Beijing 102206, People's Republic of China
[47]Peking University, Beijing 100871, People's Republic of China
[48]Qufu Normal University, Qufu 273165, People's Republic of China
[49]Renmin University of China, Beijing 100872, People's Republic of China
[50]Shandong Normal University, Jinan 250014, People's Republic of China
[51]Shandong University, Jinan 250100, People's Republic of China
[52]Shanghai Jiao Tong University, Shanghai 200240, People's Republic of China
[53]Shanxi Normal University, Linfen 041004, People's Republic of China
[54]Shanxi University, Taiyuan 030006, People's Republic of China
[55]Sichuan University, Chengdu 610064, People's Republic of China
[56]Soochow University, Suzhou 215006, People's Republic of China
[57]South China Normal University, Guangzhou 510006, People's Republic of China
[58]Southeast University, Nanjing 211100, People's Republic of China
[59]State Key Laboratory of Particle Detection and Electronics, Beijing 100049,
Hefei 230026, People's Republic of China
[60]Sun Yat-Sen University, Guangzhou 510275, People's Republic of China
[61]Suranaree University of Technology, University Avenue 111, Nakhon Ratchasima 30000, Thailand
[62]Tsinghua University, Beijing 100084, People's Republic of China
[63a]Turkish Accelerator Center Particle Factory Group, Istinye University, 34010, Istanbul, Turkey
[63b]Near East University, Nicosia, North Cyprus, 99138, Mersin 10, Turkey
[64]University of Bristol, H. H. Wills Physics Laboratory, Tyndall Avenue, Bristol, BS8 1TL, United Kingdom
[65]University of Chinese Academy of Sciences, Beijing 100049, People's Republic of China
[66]University of Groningen, NL-9747 AA Groningen, The Netherlands
[67]University of Hawaii, Honolulu, Hawaii 96822, USA
[68]University of Jinan, Jinan 250022, People's Republic of China
[69]University of Manchester, Oxford Road, Manchester, M13 9PL, United Kingdom
[70]University of Muenster, Wilhelm-Klemm-Strasse 9, 48149 Muenster, Germany
[71]University of Oxford, Keble Road, Oxford OX13RH, United Kingdom
[72]University of Science and Technology Liaoning, Anshan 114051, People's Republic of China
[73]University of Science and Technology of China, Hefei 230026, People's Republic of China
[74]University of South China, Hengyang 421001, People's Republic of China
[75]University of the Punjab, Lahore-54590, Pakistan
[76a]University of Turin and INFN, University of Turin, I-10125, Turin, Italy
[76b]University of Eastern Piedmont, I-15121, Alessandria, Italy
[76c]INFN, I-10125, Turin, Italy
[77]Uppsala University, Box 516, SE-75120 Uppsala, Sweden
[78]Wuhan University, Wuhan 430072, People's Republic of China
[79]Yantai University, Yantai 264005, People's Republic of China
[80]Yunnan University, Kunming 650500, People's Republic of China
[81]Zhejiang University, Hangzhou 310027, People's Republic of China
[82]Zhengzhou University, Zhengzhou 450001, People's Republic of China

[†]Deceased.
[a]Also at the Moscow Institute of Physics and Technology, Moscow 141700, Russia.
[b]Also at the Novosibirsk State University, Novosibirsk, 630090, Russia.
[c]Also at the NRC "Kurchatov Institute," PNPI, 188300, Gatchina, Russia.
[d]Also at Goethe University Frankfurt, 60323 Frankfurt am Main, Germany.
[e]Also at Key Laboratory for Particle Physics, Astrophysics and Cosmology, Ministry of Education; Shanghai Key Laboratory for Particle Physics and Cosmology; Institute of Nuclear and Particle Physics, Shanghai 200240, People's Republic of China.
[f]Also at Key Laboratory of Nuclear Physics and Ion-beam Application (MOE) and Institute of Modern Physics, Fudan University, Shanghai 200443, People's Republic of China.
[g]Also at State Key Laboratory of Nuclear Physics and Technology, Peking University, Beijing 100871, People's Republic of China.
[h]Also at School of Physics and Electronics, Hunan University, Changsha 410082, China.

[i]Also at Guangdong Provincial Key Laboratory of Nuclear Science, Institute of Quantum Matter, South China Normal University, Guangzhou 510006, China.

[j]Also at MOE Frontiers Science Center for Rare Isotopes, Lanzhou University, Lanzhou 730000, People's Republic of China.

[k]Also at Lanzhou Center for Theoretical Physics, Lanzhou University, Lanzhou 730000, People's Republic of China.

[l]Also at the Department of Mathematical Sciences, IBA, Karachi 75270, Pakistan.

[m]Also at Ecole Polytechnique Federale de Lausanne (EPFL), CH-1015 Lausanne, Switzerland.

[n]Also at Helmholtz Institute Mainz, Staudinger Weg 18, D-55099 Mainz, Germany.

[o]Also at Hangzhou Institute for Advanced Study, University of Chinese Academy of Sciences, Hangzhou 310024, China.